remote sensing

MDPI

Article

HydroSAR: A Cloud-Based Service for the Monitoring of Inundation Events in the Hindu Kush Himalaya

Franz J. Meyer [1,2,*,†], Lori A. Schultz [3,†], Batuhan Osmanoglu [4,†], Joseph H. Kennedy [2,†], MinJeong Jo [4,5,†], Rajesh B. Thapa [6,†], Jordan R. Bell [3], Sudip Pradhan [6], Manish Shrestha [6], Jacquelyn Smale [2], Heidi Kristenson [2], Brooke Kubby [1] and Thomas J. Meyer [1]

1 Geophysical Institute, University of Alaska Fairbanks, Fairbanks, AK 99775, USA
2 Alaska Satellite Facility, University of Alaska Fairbanks, Fairbanks, AK 99775, USA; hjkristenson@alaska.edu (H.K.)
3 NASA Marshall Space Flight Center, Huntsville, AL 35812, USA; lori.a.schultz@nasa.gov (L.A.S.)
4 NASA Goddard Space Flight Center, 8800 Greenbelt Rd, Greenbelt, MD 20771, USA
5 University of Maryland, Baltimore County, Baltimore, MD 21250, USA
6 International Centre for Integrated Mountain Development, G.P.O. Box 3226, Lalitpur 44700, Nepal; rajesh.thapa@icimod.org (R.B.T.)
* Correspondence: fjmeyer@alaska.edu; Tel.: +1-907-474-7767
† These authors contributed equally to this work.

Abstract: The Hindu Kush Himalaya (HKH) is one of the most flood-prone regions in the world, yet heavy cloud cover and limited in situ observations have hampered efforts to monitor the impact of heavy rainfall, flooding, and inundation during severe weather events. This paper introduces HydroSAR, a Sentinel-1 SAR-based hazard monitoring service which was co-developed with in-region partners to provide year-round, low-latency weather hazard information across the HKH. This paper describes the end user-focused concept and overall design of the HydroSAR service. It introduces the main processing algorithms behind HydroSAR's broad product portfolio, which includes qualitative visual layers as well as quantitative products measuring the surface water extent and water depth. We summarize the cloud-based implementation of the developed service, which provides the capability to scale automatically with the event size. A performance assessment of our quantitative algorithms is described, demonstrating the capabilities to map the flood extent and water depth with an accuracy of >90% and <1 m, respectively. An application of the HydroSAR service to the 2023 South Asia monsoon seasons showed that monsoon floods peaked near 6 August 2023 and covered 11.6% of Bangladesh in water. At the peak of the flood season, nearly 13.5% of Bangladesh's agriculture areas were affected.

Keywords: SAR; hazard monitoring; cloud computing; Sentinel-1; flooding; Hindu Kush Himalaya

Citation: Meyer, F.J.; Schultz, L.A.; Osmanoglu, B.; Kennedy, J.H.; Jo, M.; Thapa, R.B.; Bell, J.R.; Pradhan, S.; Shrestha, M.; Smale, J.; et al. HydroSAR: A Cloud-Based Service for the Monitoring of Inundation Events in the Hindu Kush Himalaya. *Remote Sens.* **2024**, *16*, 3244. https://doi.org/10.3390/rs16173244

Academic Editor: Magaly Koch

Received: 27 May 2024
Revised: 25 August 2024
Accepted: 27 August 2024
Published: 1 September 2024

1. Introduction

Floods are considered the most significant natural disaster affecting the low-lying floodplains of the Hindu Kush Himalaya (HKH) from the perspective of their frequency, financial cost, and impact on the population and socioeconomic activities [1]. For example, the 2019 monsoon season affected 7.3 million people, caused 119 fatalities, and displaced an estimated 308,000 people in Bangladesh alone. The same event also caused floods and landslides across Nepal and displaced more than 1.8 million people in the northern reaches of India [2].

A review of past studies of flooding events in the HKH published in [3] concluded that floods in the region cannot be completely controlled, and efforts should be directed toward reducing flood vulnerability and mitigating impacts through improved flood risk management. To accomplish efficient and effective flood risk management, near real-time information on the inundation extent, water depth, and impacts on agriculture are necessary to guide appropriate disaster risk reduction activities [4].

Regularly acquired, weather-independent synthetic aperture radar (SAR) observations such as those from the ESA's Sentinel-1 [5] and the upcoming NASA-ISRO SAR (NISAR) [6] missions have the potential to meet this critical data need. Previous case studies have identified SAR as a useful dataset for mapping floods and other weather-related hazards [7–11], yet novel data processing approaches are still needed to cope with the large data volumes associated with SAR and enable the automatic generation of hazard information at a low latency and across large spatial scales.

The increasing availability and reduced latency of SAR observations has generated growing interest in the development of such automatic flood extent monitoring algorithms. The German Aerospace Center's (DLR) Center for Satellite-Based Crisis Information (ZKI) developed a thresholding algorithm to facilitate event-based flood water extent monitoring from Sentinel-1 and TerraSAR-X SAR data [7,12]. Similar thresholding techniques were also developed by a variety of other teams [4,13,14] to provide flood extent information for individual events in China, Bangladesh, and the Mekong Delta. These papers show that thresholding techniques are applicable to areas with vegetation properties similar to the HKH. A recent work published in [15] developed an automatic system for flood extent and flood duration mapping using multi-sensor satellite observations. This system is based on four processing chains for the derivation of flood extents from Sentinel-1 and TerraSAR-X radar as well as from optical Sentinel-2 and Landsat satellite data.

A literature search more specifically focused on SAR-based flood mapping in the HKH found a growing number of publications which applied SAR to map individual events or perform retrospective flood assessments. Most of these papers relied on Sentinel-1 data as a resource and use either thresholding, change detection, or clustering methods to identify open water.

The authors of [16] applied the automatic, bimodal Otsu thresholding approach with Sentinel-1 SAR data to analyze a 2020 flooding event in northern India. Thresholding was also used in a paper focused on the 2019 flood season in Bangladesh [17]. The authors used Landsat-8 images to manually select a threshold which separated water from non-water pixels in Sentinel-1 SAR scenes.

A paper focused on the 2020 Bangladesh monsoon season used an unsupervised clustering algorithm to identify open water pixels in Sentinel-1 images, resulting in pre-flood and mid-flood water extent maps of the country [18]. While their approach yielded good results, many processing steps remained manually performed, preventing more automatic, large-scale application of the algorithm.

Change detection between pre- and mid-flood Sentinel-1 image pairs was used in [19] as part of a multi-sensor retrospective analysis of the maximum flood extents in recent Bangladesh monsoon seasons. Their approach calculated the differences between pre- and mid-flood Sentinel-1 images and then applied the change detection and thresholding (CDAT) approach [8] to identify flood water pixels. A similar change detection approach was also used in [20] to study flooding in the Ganga-Brahmaputra basin. Both of these papers focused on case studies and were not aimed at continuous, large-scale monitoring.

In addition to these papers on flood extent mapping, there is also a growing body of work related to flood depth estimation from SAR remote sensing data. Most papers on this topic use a workflow where the water extent is mapped first, followed by a depth estimation step which is based on intersecting the identified water bodies with a digital elevation model (DEM). In [21], the lowest elevation within an identified water-covered area was used as a reference to scale the topographic height to the water depth. The auhtors of [22] used the approach in [23], where the boundary of a flooded area was first extracted and intersected with the DEM. A 3D surface model was then interpolated, and the flood depth was derived by calculating the difference between the 3D surface and the DEM. A similar approach was also used in [24].

Despite these recent advances, most recent works remain focused on case studies rather than operational monitoring. While some operational services have emerged, they are often characterized by a rather narrow product portfolio (e.g., surface water extent

only), providing only limited information about an ongoing event. Furthermore, most existing systems lack a scalable computing architecture, limiting their ability to continue to provide low-latency information as the size of an event increases. Lastly, many current efforts do not emphasize the co-development and transitioning of developed technology to an in-region partner when defining product portfolios, processing solutions, and delivery mechanisms of their services. This may limit the impact of their work on decision-making practices in a specific target region.

In this paper, we introduce HydroSAR, a cloud-based SAR data analysis service which was co-developed with end user partners for the monitoring of hydrometeorological events in the Hindu Kush Himalaya. Funded through a NASA SERVIR Applied Science Team grant, HydroSAR includes a series of SAR-based value-added products for the monitoring of surface hydrology (image time series, flood extent, water depth, and affected agriculture) in a region. Product algorithms were selected, adapted, and operationalized based on a review of the recent literature and in collaboration with end user partners in the flood-prone Hindu Kush Himalaya. The goal of HydroSAR was to develop a more complete set of hazard data layers than most comparable systems, enabling simultaneous assessment of the surface water extent, water depth, and flood impacts on agriculture.

After illustrating the motivation of our work with a summary of the flood mapping needs in the HKH (Section 2), we discuss our co-development strategy, which is implemented to ensure that HydroSAR meets the needs of the end users in the region (Section 3). The selected HydroSAR product portfolio and product algorithms are summarized in Section 4. After presenting our visualization and data sharing concepts in Section 5, Section 6 introduces the cloud-based implementation of HydroSAR, providing the capability to scale automatically with the event size and enabling near real-time access to the production of actionable information even for events of extremely large spatial scales. Section 7 provides a performance assessment of HydroSAR product algorithms by comparing SAR-derived products to reference information provided by in-region partners or derived from different sensors. Finally, we demonstrate the impact of our service by applying HydroSAR products to the 2023 monsoon season (Section 8). A summary and outlook conclude this paper.

2. Flood Mapping Needs in the HKH

The HKH region extends over 3500 km, encompassing Myanmar in the east and reaching to Afghanistan in the west (dark blue region in Figure 1). The region spans over 3,441,000 km^2, covering about 2.9% of the global land mass and 18% of the global mountain regions [2]. With its high variability in topography, the region hosts 10 large rivers, including the Mekong, Yangtse, Yellow, Salween, Irrawady, Brahmaputra, Ganges, Tarim Indus, and Amu Darya rivers, making large areas of Afghanistan, Bangladesh, India, Nepal, and Pakistan susceptible to inundation by floodwaters during every rainy season [2]. Among these countries, Bangladesh has been experiencing record-high floods almost every year due to Bangladesh's unique geographical setting as the most downstream country in the HKH [25]. On average, about 26,000 km^2 of Bangladesh is inundated every year during the peak of monsoon season [1]. Floods can persist for several weeks in some regions of the country.

Rapid change during the recent global warming period has altered meteorological and hydrological extreme events in the HKH, giving rise to a further increase in the frequency of flood hazards [2,8]. Today, large areas of Bangladesh, Bhutan, India, Nepal, and Pakistan are subject to frequent extreme weather events, creating a hazard environment where floods can damage infrastructure and threaten livelihoods.

Climate change-enhanced variability in precipitation patterns and associated increases in the occurrence of floods have also affected agricultural productivity and income across the HKH and led to increased vulnerability and uncertainty in food and nutrition security [26]. A survey of disaster impacts between 2000 and 2022 showed that floods have

become the most common hazard in the HKH [3], accounting for 47% of people affected and 49% of the annual economic loss caused in the region (Figure 1).

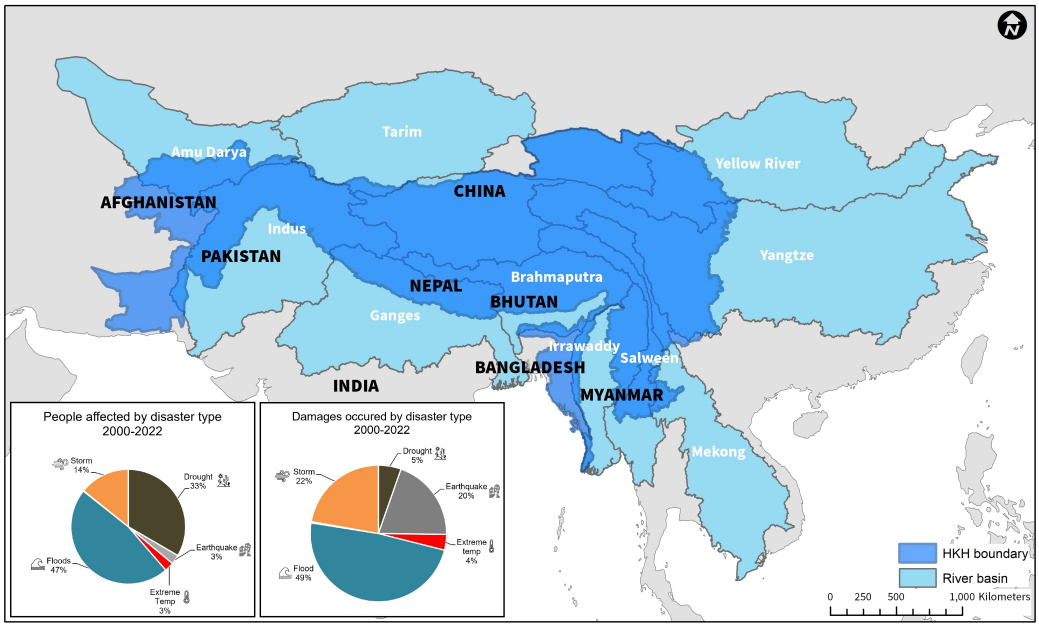

Figure 1. Survey of disaster impacts in the HKH using data from the international disaster database EM-DAT (https://www.emdat.be/; accessed on 5 March 2024). The data show that flooding events are the predominant hazard affecting communities in the region, resulting in the majority of economic damages. The boundary of the HKH is shown in dark blue. Light blue background shows HKH-associated river basins.

A key element of weather- and climate-related disaster risk reduction (DRR) is near real-time access to actionable information on the surface water extent, water depth, and event impacts on settlements and agriculture [27]. Unfortunately, the HKH lacks in situ observations for monitoring the impact of heavy rainfall, flooding, and inundation during severe weather events due to both the remoteness of the region as well as limited technical and economic capacities.

3. Co-Developing an Inundation Monitoring Service for the HKH

As for any SERVIR-funded service, co-development and transitioning of developed technology to an in-region partner organization was a central part of the HydroSAR service development cycle. To ensure the HydroSAR service is sustainable and meets the end user needs, we utilized a SERVIR-pioneered iterative co-development process, where end user agencies and the HydroSAR project team jointly agreed on the project specifications and created a method to monitor the impact of the service with a monitoring, evaluation, and learning (MEL) workflow [28]. As displayed in Figure 2, this workflow integrates end user needs and preferences throughout a service development cycle until eventual delivery of a final service is achieved.

As indicated by the arrows in Figure 2, each co-development cycle of this workflow follows a sequence of end user need assessment, service design, and service delivery. At the end of each cycle, a service evaluation and impact assessment step is performed, from which a subsequent co-development cycle is initiated until service convergence is achieved. End user engagement is further enabled through regular end user consultation and capacity building workshops (center of Figure 2) held throughout the project's duration.

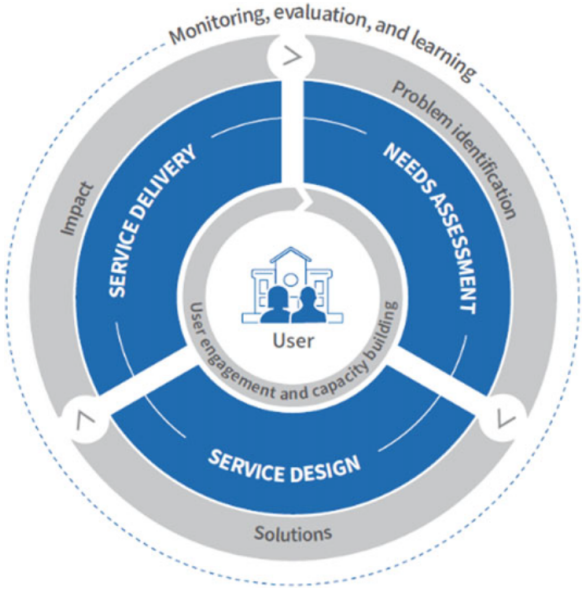

Figure 2. NASA SERVIR iterative co-development workflow used in HydroSAR service development to ensure that HydroSAR is sustainable and meets the end user's needs. Each co-development cycle of this workflow follows a sequence of end user needs assessment, service design, and service delivery. At the end of each cycle, a service evaluation and impact assessment step is performed from which a subsequent co-development cycle is initiated until service convergence is achieved.

To implement this co-development workflow, we worked most closely with the International Centre for Integrated Mountain Development (ICIMOD), an intergovernmental knowledge and learning center that develops and shares research with the eight regional member countries of the HKH: Afghanistan, Bangladesh, Bhutan, China, India, Myanmar, Nepal, and Pakistan [29]. As one of the core member organizations of the HydroSAR project, and as the hub of SERVIR in the Hindu Kush Himalaya, ICIMOD (https://servir.icimod.org/; accessed on 26 August 2024) facilitated end user consultations, training activities with partner countries, in situ data collection, and field verifications throughout the project development phase. Together with the ICIMOD, we conducted several consultation meetings and training activities, inviting relevant stakeholders working on flood management practices. The participants in the workshops comprised government and non-government agencies from Bangladesh, Bhutan, and Nepal. Stakeholder feedback collected during these consultation meetings and capacity building events was used to refine the product specifications and delivery mechanisms of the HydroSAR service.

The ICIMOD is now the host of the completed and operational HydroSAR service and is continuing to evaluate the impact of HydroSAR technology through existing partnership arrangements with national agencies in the HKH.

4. HydroSAR Product Portfolio and Product Algorithms

Based on the information in Section 2, developing a SAR-based weather hazard monitoring system capable of providing low-latency flood impact information on a regional scale and during all weather conditions is a necessity [30] for the HKH [4].

Therefore, in collaboration with the end user partners of ICIMOD, we designed the HydroSAR service to provide near real-time access to a comprehensive set of SAR-derived information products to allow assessment of the surface water extent, water depth, and flood impacts on agriculture. Our coordinated set of hazard information products, along with their data dependencies, is shown in Figure 3. The product portfolio combines visual aids to be used by analysts with quantitative products on flood status and flood impact.

All HydroSAR products were generated in cloud-optimized GeoTIFF (CoG) format so that data could be efficiently accessed and distributed in the cloud (Section 6). They

were presented to analysts and other end-users through a dedicated web portal discussed in Section 5.

The purpose and implementation of each individual product is described in the following subsections. For the purpose of brevity, we will focus on the intermediary layers (HAND), visual aids (RTC30 and RTC30-Color), and quantitative flood water products (HYDRO30 and WD30) in this paper, for which automatic processing workflows are implemented. While HydroSAR also includes an agriculture extent product (AG30), this product is not yet included in the HydroSAR web portal and will not be discussed here. Readers interested in the concepts behind AG30 may refer to [31] for more information.

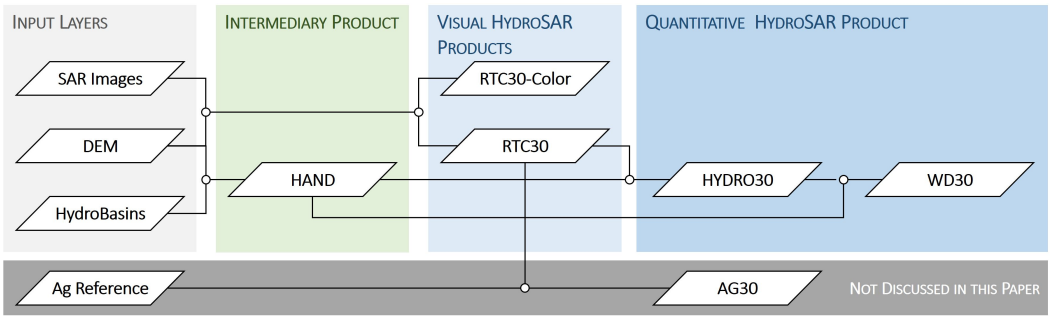

Figure 3. Portfolio of flood hazard products created by HydroSAR to support the analysis of flood status and impact in the HKH. Input data are shown on the left. The green column shows the intermediary data layers needed to generate the final visual and quantitative HydroSAR products shown on the right side of the figure. Lines indicate workflows and dataset dependencies. The HydroSAR agriculture extent product AG30 is not discussed in this paper but is included for completeness.

4.1. Input Data

Input data for HydroSAR are shown in Figure 3 and consist of SAR data, digital elevation model (DEM) information, and ancillary information such as hydrobasin and agriculture reference data. Data used for product validation are presented in Section 7.

SAR data used in HydroSAR consists of NASA-managed Sentinel-1 SAR data holdings at the Distributed Active Archive Center (DAAC) of NASA's Alaska Satellite Facility (ASF). The Sentinel-1 C-band SAR constellation has been providing free and open, globally observed SAR data since 2014 and observing all global land masses at high sampling rates. Sentinel-1 provides complete coverage of the HKH once every 8–10 days. Data are typically processed and delivered to the ASF's DAAC within 6 h after image acquisition. With its global acquisition strategy, its cloud-free imaging capabilities, and its comparably low latency data delivery, Sentinel-1 provides an excellent basis for HydroSAR's inundation mapping goals.

The DEM data used in this project consisted of the 30 m resolution Copernicus GLO-30 digital elevation model [32]. This freely-accessible resource is based on acquisitions of the TanDEM-X mission, a constellation of two satellites flown with the goal to generate a global DEM [33]. GLO-30 is a validated DEM [34] and provides consistent-quality topographic information across our area of interest. The HydroSAR processor accesses the GLO-30 DEM directly in AWS through its Registry of Open Data program.

Beyond these data types, We used ancillary information about watersheds and land cover in some of our processing routines (see Section 4.2.1). Hydrobasin information was accessed from the HydroSHEDS database [35], which offers a suite of global digital data layers in support of hydro-ecological research and applications worldwide. The landcover information used in HydroSAR originated from the Copernicus Global Land Monitoring Service [36].

4.2. Intermediary Data Products and Visual Aids

4.2.1. Height above Nearest Drainage

HAND is a terrain descriptor calculated from a hydrologically coherent DEM [37]. The HAND model normalizes topography based on the local relative heights observed along a drainage network (Figure 4). In the HAND grid, each pixel value indicates the vertical distance between a specific location and its nearest drainage stream. HAND can be calculated for individual hydrological basins such as HydroSHEDS [35] under the assumption that each basin is self-contained. HAND can also be calculated independent of the hydrological basin information in a tiled approach when calculating over large regions. In this case, a buffer is used to eliminate any edge effects due to tiling.

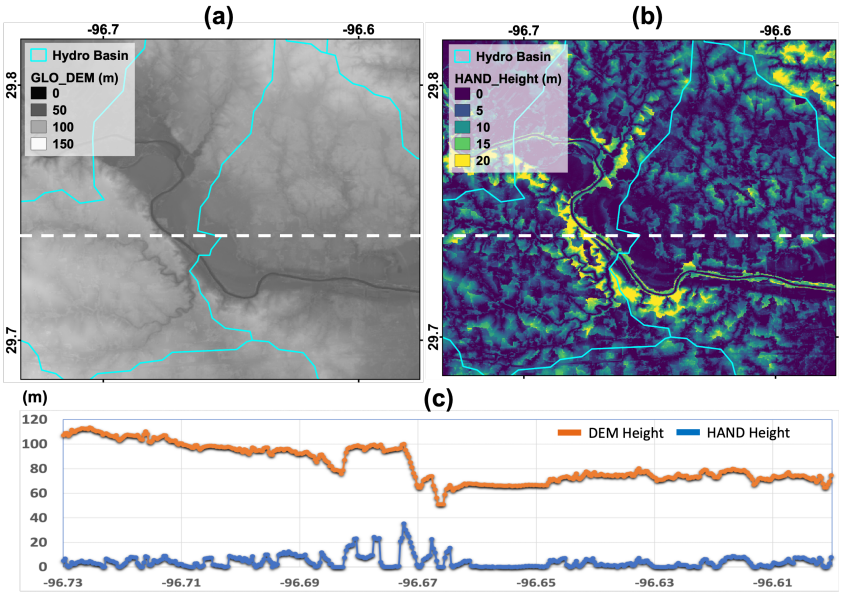

Figure 4. An example of topographic heights and the HAND model: (**a**) Copernicus GLO−30 DEM; (**b**) HAND model height generated from the DEM; and (**c**) height comparison between the source DEM and the HAND model along a transect, indicated by the dashed white line in the sub−figures (**a**,**b**).

Regardless of the domain, HAND calculation is performed the same way. First, the provided input DEM is conditioned to be hydrologically correct. This is achieved by filling in depressions, where a cell region has a much lower value than its surrounding neighbors. We then resolve the flat areas to identify drainage basins. With the drainage basins identified, the flow directions can be calculated, allowing for the generation of routing patterns, which are used to calculate the total accumulations showing the number of pixels draining into one another. At the final step, these accumulation values are used to calculate the HAND using an accumulation threshold and eight-directional flow, also known as D8. The accumulation threshold determines the drainage mask based on the total accumulation for a given cell, directly impacting the output. Figure 4 illustrates the relationship between the source DEM and the HAND product. Upon comparing the heights in Figure 4c, it becomes evident that the slope and trend of the DEM were removed from the HAND product.

To determine an optimal accumulation threshold, we generated HAND solutions over the same area with various accumulation thresholds between 60 and 3500 pixels, demonstrating that the smaller the accumulation threshold, the more detailed the drainage network became. As the accumulation threshold became smaller, the river networks became more dendritic at finer scales. In order to create a globally uniform HAND, we selected an accumulation threshold of 100 pixels (corresponding to an area of about 9 ha), as this threshold allowed maintaining a close correspondence between the HAND-derived and HydroSHEDS-mapped drainage network. Our accumulation threshold was also close to

the 10 ha threshold used in [38]. The HAND was then calculated using this threshold and by leveraging the pysheds library [39].

Due to the large spatial extent of the HKH, we used a tiling scheme to calculate the HAND across our area of interest [39]. We started by defining a tiling scheme composed of 1×1 degree latitude and longitude chunks. Then, our strategy consisted of the following three steps. (1) We first buffered each 1×1 degree tile by 0.5 degrees, resulting in a 2×2 degree buffered tile with 50% overlap between neighboring tiles. We found that this 50% overlap minimized the basin boundary clipping effects and resulted in an HAND product without measurable seams at the tile boundaries. (2) We retrieved the GLO-30 DEM information for each buffered tile and computed the HAND across the 2×2 degree area. (3) Finally, we cropped the 0.5 degree overlap areas from the calculated HAND product and merge the cropped 1×1 degree tiles, resulting in a final seamless HAND product.

4.2.2. RTC30 Product

Previous research has demonstrated the benefits of radiometric terrain correction (RTC) processing for many mapping and hazard monitoring applications [10,11,40,41]. The removal of topography-induced radiometric biases (topographic shading) from SAR images aids in the visual interpretation of SAR amplitude data by analysts. Furthermore, RTC processing reduces the requirement for exact repeat acquisitions in change detection algorithms by mitigating the differences between images which are introduced by changes in the observation geometries [10].

Based on the end user input, HydroSAR's RTC30 product (Figure 5a) was designed as a 30 m RTC-processed SAR image product, and it serves as a visual aid and as an essential base dataset in the HydroSAR service. RTC30 forms the basis for most higher-level data products in the HydroSAR product portfolio (Figure 3).

We utilized the pixel area integration approach proposed by Small [42] to perform RTC processing. We chose this approach as it was reported in several studies to provide the best RTC processing accuracy [43–45]. It was also adopted by the Analysis Ready Data (ARD) working group of the Committee on Earth Observation Satellites (CEOS) as one of the recommended approaches for generating terrain-normalized radar backscatter products.

In this approach, radiometric normalization is performed by determining the actual area on the ground for every SAR resolution cell. According to [10], the average normalized backscatter coefficient σ^0 for a pixel is calculated as follows:

$$\sigma^0 = \beta^0 \cdot \frac{A_{\sigma^0_{cos}}}{A_{\sigma^0_{pa}}} \quad [dB] \tag{1}$$

with the (calibrated) radar brightness β^0, ellipsoid reference area $A_{\sigma^0_{cos}}$, and illuminated topographic pixel area $A_{\sigma^0_{pa}}$ [46]. In our algorithm, the σ^0 data from Equation (1) are further projected into the γ^0 space using the local incidence angle θ:

$$\gamma^0 = \frac{\sigma^0}{cos(\theta)} \quad [dB] \tag{2}$$

For land applications, γ^0 provides the best measure for image classification and time series analysis [46]. Single Look Complex (SLC) Sentinel-1 Interferometric Wide Swath (IW) data, along with the 30 m resolution Copernicus GLO-30 DEM, are used to generate the HydroSAR RTC30 products. For ease of integration into our cloud-based workflows, RTC-30 data are generated as cloud-optimized GeoTIFFs. For more information on the RTC algorithm's implementation, see [39]. For information on the performance of the underlying RTC algorithm, please see [42].

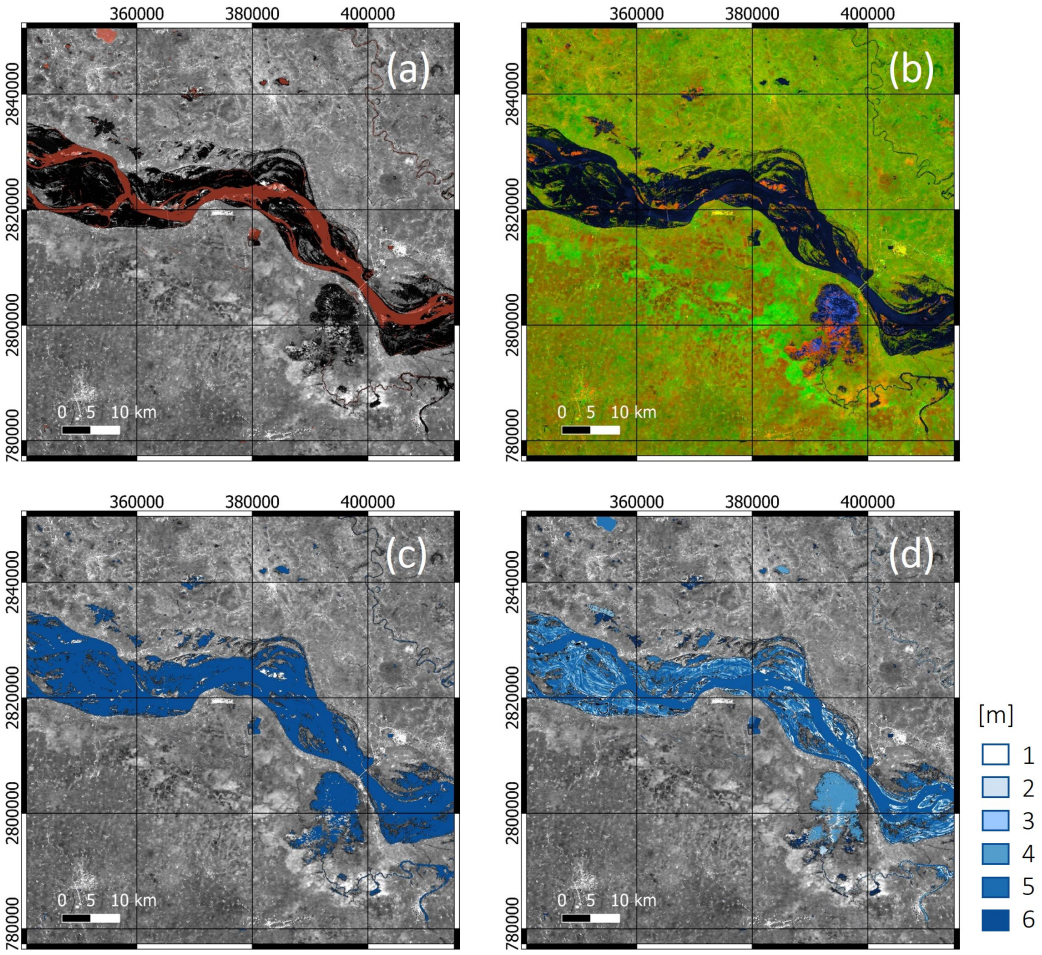

Figure 5. Example of HydroSAR flood-relevant data products for an area near the Ganges River in Bihar, India. (**a**) RTC30 product. Red shaded regions correspond to the permanent water extent in this region. (**b**) RTC30-Color image, with surface water shown in dark blue colors. (**c**) HYDRO30 surface water extent product on top of an RTC30 image. (**d**) WD30 water depth product on top of RTC30.

4.2.3. RTC30-Color

To ease the uptake of SAR data by end user organizations in the HKH, the HydroSAR team was asked to develop a product that is easy to interpret by analysts mostly familiar with optical data. In response to this request, we developed a simplified polarimetric decomposition concept based on dual-pol Sentinel-1 RTC-30 data, resulting in RGB-formatted image products which approximate the look and feel of visual band data.

This approach decomposes the co- and cross-pol signals into a simple bounce (polarized) with some volume scattering, and volume (depolarized) scattering and a simple bounce with extremely low volume-scattering components. These are assigned to the red, green, and blue color channels of an RGB composite according to

$$\begin{aligned} R &= a(VV - 3HV)^{0.5} && \text{when } HV > k \\ G &= b(HV)^{0.5} && \\ B &= c(VV)^{0.5} && \text{when } HV \leq k \end{aligned} \tag{3}$$

where a, b, and c are empirically determined to create a histogram-balanced image and k is set near the image noise floor. In the case where the volume-to-simple-scattering ratio is larger than expected for typical vegetation, such as in glaciated areas or some forest types, a teal color (green + blue) is used.

The convenience of the RGB decomposition in Equation (3) for monitoring the surface water extent stems from the fact that the blue channel is predominately associated with

surface water, providing an easy-to-understand visual aid for analysts. Figure 5b shows an RGB composite product for an area near the Ganges River in Bihar, India. In this example, water areas can be identified in blue, while vegetated areas are shown in shades of green and urban environments appear in red and orange hues.

4.3. Quantitative HydroSAR Flood Information Products

4.3.1. HYDRO30: Surface Water Extent

Our 30 m surface water extent product, HYDRO30, is a modified version of an algorithm published in [47] and performs adaptive thresholding of dual-pol RTC30 images to derive the surface water extent. A HAND layer derived from the Copernicus GLO-30 DEM is included to improve robustness. The HYDRO30 algorithm includes the following processing steps, which are also visualized in Figure 6.

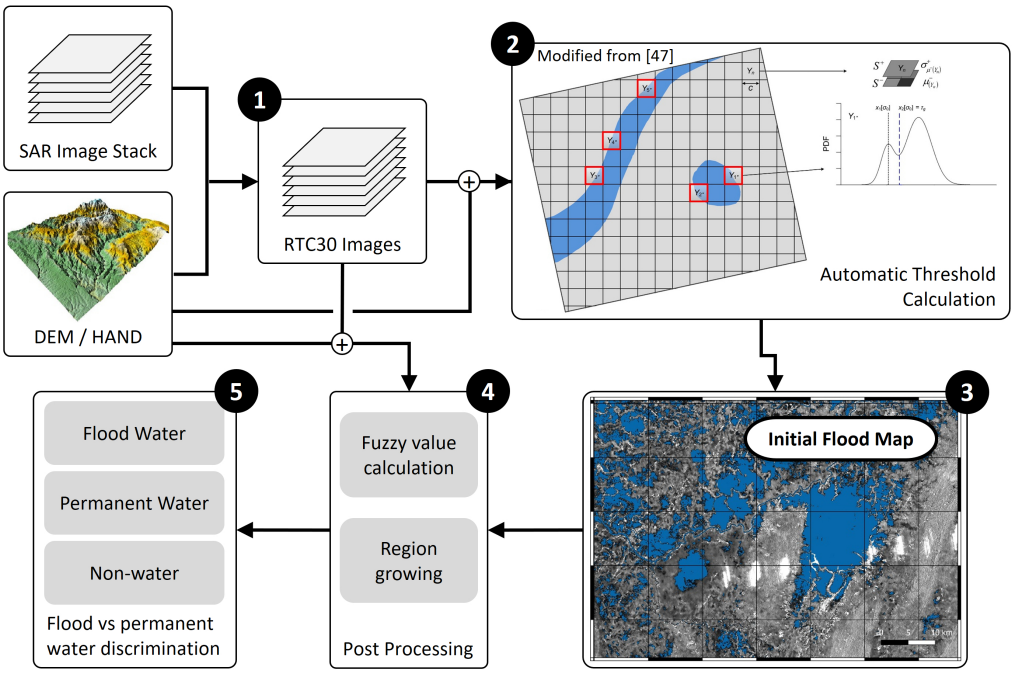

Figure 6. Summary of the HydroSAR HYDRO30 workflow, consisting of RTC generation (see Section 4.2.2), threshold calculation, selection of candidate water pixels, a post-processing refinement step, permanent and flood water discrimination, and product dissemination.

Step 1: Preparing Input Data. We used the algorithms described in Sections 4.2.1 and 4.2.2 to generate the HAND and RTC30 product layers needed for surface water threshold calculation. Due to the large data volumes associated with this regional scale monitoring effort, we performed these operations in the cloud-based processing environment (Section 6) which hosts HydroSAR. HAND data and RTC30 products were generated at a 30 m resolution and in CoG formats.

Steps 2 and 3: Adaptive Threshold Calculation. We used a modified version of the adaptive thresholding approach in [12] to identify surface water candidate pixels from the RTC30 input data. Information about the modifications we applied relative to [12] along with their motivation are provided in the individual processing step descriptions below.

Like in [12], we utilized a bi-level quadtree tile structure to ensure robust threshold calculation. We first divided the scenes into a parent level structure with a tile size of 100×100 pixels. Each parent tile was subsequently subdivided into 2×2 child objects of 50×50 pixels each.

Once this structure was created, we used the following three criteria to select the subset of parent tiles most suitable for automatic threshold calculation:

- For each parent tile, we calculated the coefficient of variation (CV) of the mean radar brightness values of its four child objects. This is a departure from [12], who used the standard deviation as a metric. We found CV to be more robust across regions with different average radar brightness. Parent tiles with high CV values are potential candidates for threshold calculation, as a high CV is expected for tiles which contain both the water and land semantic classes. Tiles which offer the highest (>95% percentile) CV were selected as candidates.
- We required the parent objects to have a mean radar brightness lower than the mean of all parent tiles. This ensured that tiles lying on the boundary between water and land areas were selected.
- To improve the robustness of the threshold calculation, we excluded parent tiles which were not in flood-prone regions. To accomplish this, we labeled the pixels with HAND elevations $\leq$15 m as unlikely to be flooded. This threshold was based on studies which found that average flood depths of up to 10 m are possible in the region [48]. We added an additional buffer of 5 m to ensure that most tiles which could include flood water were retained for further analysis. This is a second departure from [12], where the DEM instead of the HAND was used to identify tiles which could be discarded. As the HAND is a hydrologically conditioned dataset, we found it to be a more suitable and robust variable to identify tiles which were not in flood-prone regions. Tiles were only considered if less than 20% of their pixels were identified as not being flood-prone.

We selected the $N = 5$ best tiles for threshold calculation, using the CV of the mean radar brightness values as a ranking metric. We calculated the threshold values for each of these $N = 5$ tiles using expectation maximization [11] and defined the best scene-wide classification threshold τ_g as the arithmetic mean of the five individual thresholds. The use of expectation maximization rather than Otsu [16] thresholding is a third departure from the work in [12]. We made this switch as we found the radar brightness distributions for many image tiles to be trimodal rather than bimodal. This caused occasional classification errors when using an Otsu classifier, which expects bimodal behavior.

Using this dynamically calculated threshold, both the VV and VH bands of the Sentinel-1 RTC30 data were classified into water and no-water classes, and the classification maps derived for VV and VH were combined to create a combined surface water candidate mask.

Step 4: Fuzzy Logic Post-Processing. Similar to [47], fuzzy logic post-processing was used to identify and remove false water defections from the surface water candidate mask. Fuzzy rules were established for the (1) radar brightness, (2) HAND elevation, (4) surface slope, and (4) water patch size. The rule set was designed to ensure that dark pixels with low HAND elevations and low surface slopes received higher likelihoods to be true flood pixels [49]:

1. **RCS**: $\left\{ \begin{matrix} x_{u,RCS} & = & \tau_g \\ x_{l,RCS} & = & \mu_{\sigma^0(\tau_g)} \end{matrix} \right\}$ with $\sigma^0(\tau_g)$ = RCS of initial flood candidate pixels;
2. **HAND**: $\left\{ \begin{matrix} x_{u,HAND} & = & \mu_{HAND(water)} + 3 \cdot \sigma_{HAND(water)} \\ x_{l,HAND} & = & \mu_{HAND(water)} \end{matrix} \right\}$;
3. **Surface slope** α: $\left\{ \begin{matrix} x_{u,\alpha} & = & 0^\circ \\ x_{l,\alpha} & = & 15^\circ \end{matrix} \right\}$;
4. **Area** A: $\left\{ \begin{matrix} x_{u,A} & = & 10px \\ x_{l,A} & = & 3px \end{matrix} \right\}$.

Our second fuzzy rule deviated from the approach in [47], which used DEM heights rather than HAND. As a hydrologically conditioned variable, we found the HAND to lead to more hydrologically relevant fuzzy weights and fewer rejections of true water pixels.

Fuzzy membership functions were calculated for each indicator using Z-shaped activation functions. Membership scores were averaged, and a threshold of 0.45 was applied to remove false detections.

Step 5: Discrimination of Permanent and Flood-Related Water. In a final step, we separated perennial water from flood-related surface water using reference data from the

Joint Research Centre's global surface water dataset. The initial version of this dataset was produced using Landsat images at a 30 m resolution acquired between 1984 and 2021 [50], and it is currently updated annually.

HYDRO30 products were operationally created across the HKH as part of the HydroSAR service. An example of a HYDRO30 product is shown in Figure 5c, and a performance assessment is presented in Section 7.

4.3.2. WD30: Water Depth

The HydroSAR 30 m water depth product WD30 is computed based on HAND and the HYDRO30 water extent product described in Section 4.3.1. The calculation is performed separately for each independent water patch. Our WD30 workflow is shown in Figure 7a and consists of the following steps.

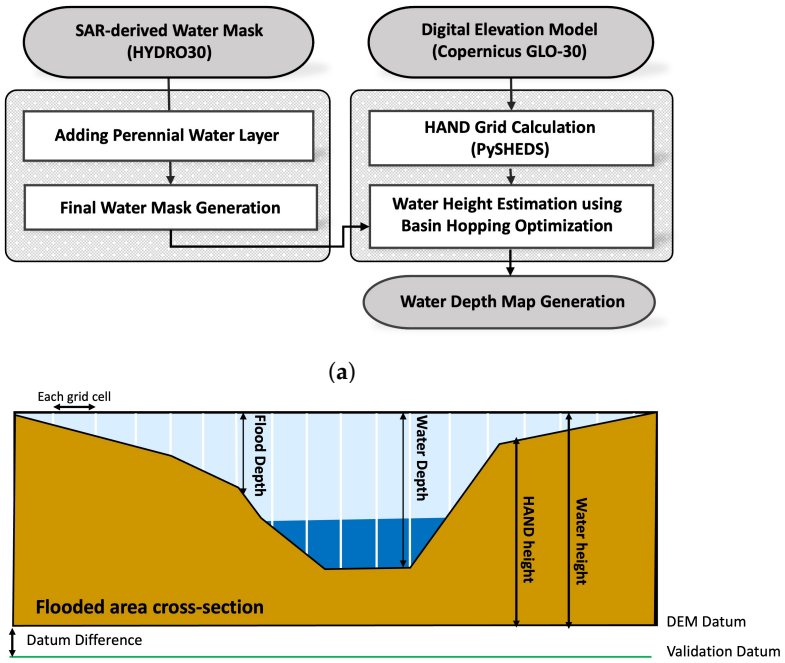

Figure 7. (**a**) The workflow of water depth estimation and (**b**) an image showing the terms used in the workflow.

Step 1: Fetching HYDRO30 and HAND from HydroSAR Cloud Storage. While any GDAL-compatible binary raster can be used to generate a water depth map, the HYDRO30 products were used as fundamental inputs for WD30 calculation. HYDRO30 and the HydroSAR HAND products were fetched from the HydroSAR cloud storage bucket to prepare for water depth derivation. HAND products were clipped to match the coverage of the HYDRO30 products.

Step 2: Integrating Water Extent Maps and Perennial Water Layer. We combined the perennial water layer mentioned in Section 4.3.1 with the observed water extent maps to ensure gap-free coverage of perennial water bodies. Gaps in the SAR-based water extent maps may have occurred due to man-made structures such as bridges or dams or due to overhanging vegetation. The primary role of the perennial water layer is to close potential gaps and connect water bodies which are expected to be connected. This was achieved by first finding the maximum percent occurrence (i.e., smallest areal extent) covering 68% of the observed water extent in the HYDRO30 product. The thresholded perennial water layer was then merged with the observed water extent. Note that the final WD30 extent matched the HYDRO30 extent if the perennial water pixels used to link connected water bodies were removed.

Step 3: Water Height Estimation using Basin Hopping. Water depths were estimated using the basin hopping algorithm [51], an iterative estimator which identifies the optimal match between the observed water extent and simulated water extent provided by the HAND grid and the maximum water height (Figure 7b). The basin hopping algorithm tries to find the best matching surface water extent by flooding HAND at different water levels and comparing the resulting extent with that of the HYDRO30 product. The search space was bounded to be between 0 and 15 m (matching the bounds used in HYDRO30; Section 4.3.1), and the basin hopping step size was set to 3 m. This basin hopping step size reduced the likelihood of the algorithm converging to a local minimum, which manifested itself as varying results in repeated basin-hopping runs, which by default had random initial seeds. Once the best-fitting water height was estimated, the water depth was calculated by subtracting the HAND from the estimated water height (Figure 7b), and any additional pixels added by the perennial water mask were removed. If desired, the product could be further masked by removing areas with permanent surface water to obtain a flood depth product rather than a water depth product. An example of a WD30 product is shown in Figure 5d. A performance assessment of this product is presented in Section 7.

5. Product Visualization and Access Mechanisms

We worked with the ICIMOD to co-develop a web portal for the visualization, analysis, and downloading of HydroSAR data products. The web application is openly available to the general public and has been used by end users for inundation assessment in the HKH since 2022 (https://geoapps.icimod.org/Floodinundation/; accessed on 26 August 2024).

In its role as an intergovernmental organization, the ICIMOD has been maintaining a number of science applications, which use Earth observation data together with ground-based observations and advanced geospatial information technology to help decision makers respond to environmental hazards in the HKH. To provide consistency across this science application portfolio (https://servir.icimod.org/science-applications/; accessed on 26 August 2024), ICIMOD developed unified service design principles which were also followed when designing the HydroSAR service (Figure 8):

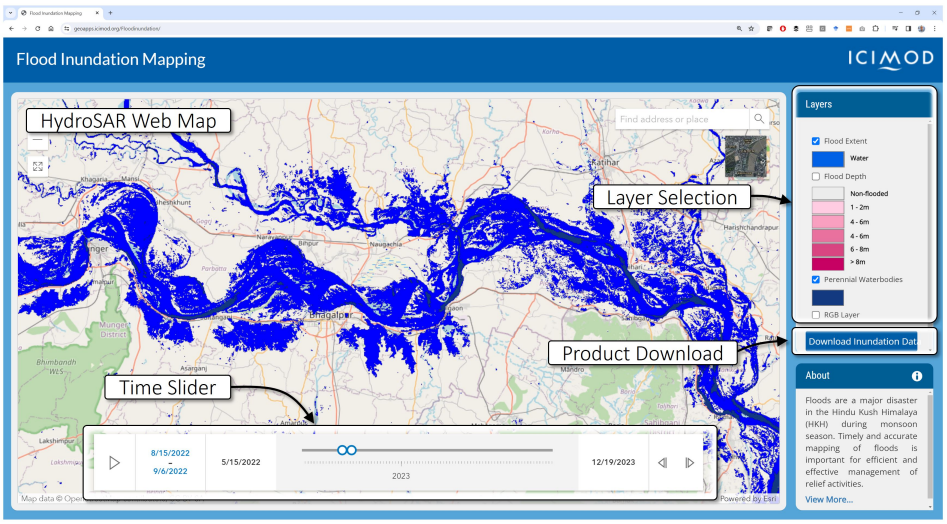

Figure 8. The HydroSAR inundation mapping web application designed and maintained by ICIMOD. The application includes webmap-based visualization of HydroSAR data products, an option to analyze changes in flood parameters over time, and the capabilities to access and download individual HydroSAR products.

- Data products are exposed to the public via a web mapping service which allows visualizing water extent and depth information in a geographic context. This web map is supported by an ArcGIS image service on the backend, making it simple to distribute HydroSAR resources to desktop, mobile, and browser applications.

- A time slider is included to support the assessment of changes in water extent and depth over time.
- A layer selector provides the capability to switch between different HydroSAR data products for cross-comparison, cross-validation, and joint hazard assessment.
- A product download feature allows users to access and download HydroSAR products over their area of interest.

Access to and the downloading of HydroSAR data products are facilitated by the ICIMOD's Regional Database System (RDS) (https://rds.icimod.org/; accessed 26 August 2024), a one-stop data portal for the HKH. The HydroSAR inundation data download tool shown in Figure 9 allows selecting HydroSAR data products by country, date range, or user-defined bounding boxes. Once a request is made, data are bundled into zip files, and a download link is sent to interested users via email.

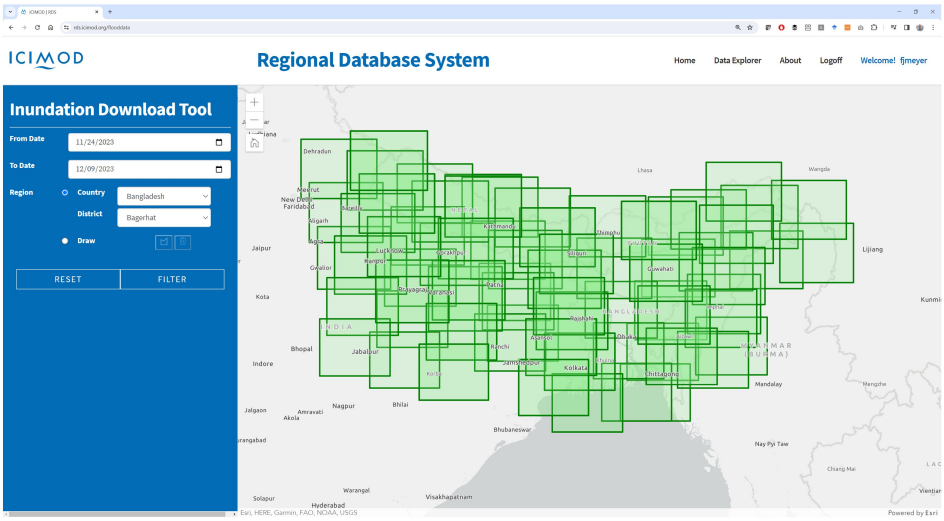

Figure 9. The HydroSAR inundation data download tool under the RDS portal. Data can be selected by country, date range, or user-drawn AOI.

6. HydroSAR Cloud Computing Environment

The HydroSAR processing algorithms presented in Section 4 are implemented in the Amazon Web Services (AWS) cloud (Figure 10) to enable rapid processing across large spatial scales [49]. This cloud approach provides an innovative, open, scalable, and sustainable processing solution for the HKH, being ready for continued operation by our in-region partners at ICIMOD. To achieve a cloud architecture that is both performant and cost effective, we partnered with NASA's Alaska Satellite Facility (ASF), which has extensive cloud development expertise from their preparations for the upcoming NASA-ISRO SAR (NISAR) mission.

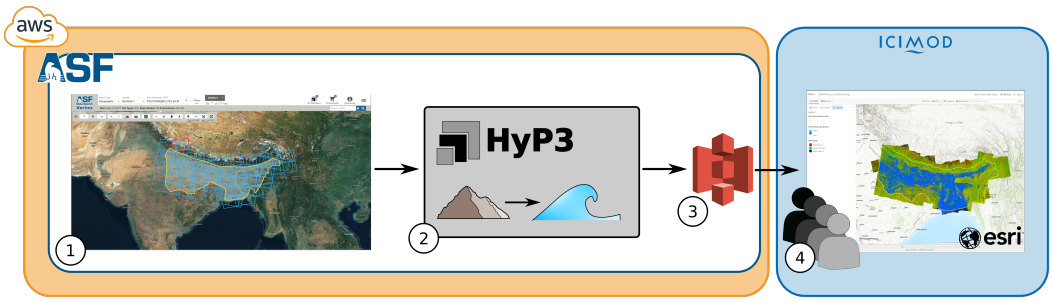

Figure 10. Cloud architecture of the HydroSAR service, including (1) integration with ASF's cloud-based archives; (2) HydroSAR product generation in the cloud using ASF HyP3; (3) temporary product storage in AWS S3; and (4) data delivery to end users via an image service.

As shown in Figure 10, HydroSAR utilizes and seamlessly integrates with two existing ASF-supported services to provide a streamlined user experience: ASF's cloud-based data archive and ASF's Hybrid Pluggable Processing Pipeline (HyP3) [52]. The resulting service is able to produce from hundreds to thousands of higher-level products an hour. ArcGIS image services are used to allow for automatic integration of data products into the HydroSAR web portal (Section 5) and for use within desktop GIS environments at HKH partner organizations.

The cloud architecture of HydroSAR includes the following components (Figure 10):

1. **Integration with ASF's cloud-based archives** is achieved by co-locating the HydroSAR services with ASF's archives in AWS region us-west-2. This design reduces data movement and enables rapid in-region data access without requiring data downloading.
2. **Cloud-based HydroSAR product generation** is facilitated by ASF HyP3, a cloud-scaling service allowing science algorithms to run automatically from regional to global scales. Mature HydroSAR workflows are integrated into HyP3 using Docker containers [53] and are run automatically whenever new SAR data over an area of interest hits the ASF archive.
3. **HydroSAR cloud storage** is provided in the form of an AWS S3 storage bucket. HydroSAR products are deposited in this bucket immediately after product generation and stored temporarily until pickup by ICIMOD.
4. **Product delivery** to end users is facilitated by ICIMOD. Using a cron job scheduler utility, ICIMOD fetches new HydroSAR products on a daily basis from the project's maintained S3 bucket for inclusion into their local database. As discussed in Section 5, ICIMOD serves out HydroSAR data to its end users via an image service-supported web interface.

The HydroSAR service has been using this implementation since 2022 to generate flood hazard information across the HKH and serve these products to end users in Nepal, Bangladesh, Bhutan, and northern India.

7. Validation of Quantitative HydroSAR Information Layers

Our strategy for evaluating the performance of HydroSAR data products includes two different approaches. For HYDRO30, we derived formal performance metrics by comparing the HydroSAR products to estimates derived from other sensors or other approaches. For WD30, we evaluated our products by comparing them to water depth field observations provided by partners in the region.

7.1. Validating HYDRO30

We used a quantitative approach and a qualitative approach to evaluate the performance of HYDRO30 products, including (1) a quantitative comparison of HYDRO30 with water extent information extracted from multispectral imagery and (2) a qualitative cross-comparison with water extents from a Google-developed flood forecasting model [54].

For our quantitative comparison to multispectral data, we selected near-simultaneous observations of Sentinel-1 SAR and (cloud-free) Sentinel-2 or Landsat-8 images over flood-affected regions. We selected these two multispectral sensors as references as they are of similar resolutions to Sentinel-1 and established methods for detecting surface water from their data exist.

Due to persistent cloud coverage over the HKH during monsoon season, we could not perform quantitative comparisons to multispectral data over our main area of interest. Instead, we validated HYDRO30 against multispectral data for an area along the Missouri River at the corner of Nebraska, Kansas, and Missouri in the USA (Figure 11). We focused on data from 2019 for this analysis, as the midwestern US experienced a major flooding event in 2019 which was fueled by heavy rainfall and melting snow [55]. This flooding event was the longest-lasting flood since 1927 in the region, giving the opportunity to study HYDRO30's performance as the flood progressed.

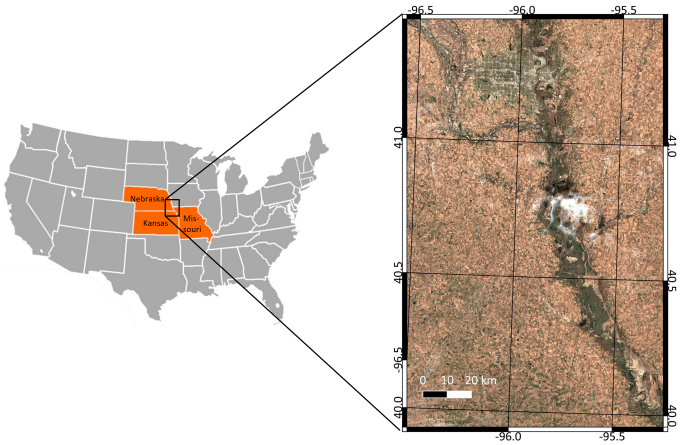

Figure 11. Validation area used to compare HYDRO30 water extent products to water extent maps derived from Landsat-8 and Sentinel-2. The site included the Missouri River at the corner of Nebraska, Kansas, and Missouri in the USA.

A total of 17 date pairs of SAR and optical (Landsat-8 and Sentinel-2) images were selected for cross-validation, with the dates falling between April and October 2019. These data pairs were selected based on a few factors. Firstly, we required that the SAR and optical images were acquired within a 5 day window of each other. This ensured that both datasets measured comparable surface water extents. Secondly, we required that the optical images contained less than 20% cloud cover in order to reduce discrepancies based on cloud cover and cloud shadows.

We derived the water extent from Sentinel-1 using the HYDRO30 algorithm and from multispectral data using the established modified normalized difference water index (mNDWI) [56] approach. We compared the water extent information from both sensor types and calculated the skill scores to evaluate HYDRO30's products. Our skill scores included accuracy ($A = ((TP+TN))/T$) and precision ($P = TP/(TP+FP)$), with TP meaning true positive, TN meaning true negative, FP meaning false positive, FN meaning false negative, and T meaning the total population.

An example of this approach is shown in Figure 12. Here, the HYDRO30 water extent information is shown in the left panel, while the water extent mapped from optical data using the nNDWI is shown in the center. The right panel is a comparison of the produced water extent information, with blue areas indicating agreement, red regions indicating missed detections by HYDRO30, and light blue areas indicate water detections in HYDRO30 which were not found in the optical data. The example in Figure 12 demonstrates that HYDRO30 typically matched optical reference data with high accuracy ($A = 98\%$ and $P = 86\%$). Additional examples of Sentinel-1 (S1) and optical image comparisons are presented in Table 1, showing overall consistent water mapping skills. Throughout the 17 data pairs in our analysis, we saw an average accuracy of $A = 99\%$ and average precision of $P = 79\%$.

As cloud cover limits the usability of multispectral images during most of the HKH monsoon season, we were unable to perform a quantitative comparison to multispectral data for this region. Instead, we augmented our quantitative analysis along the Missouri River with a qualitative comparison to Google-provided flood forecasts which are available for some parts of the HKH. Figure 13a shows a comparison of the HYDRO30 data (blue) and Google flood forecasts (hash pattern) for the Kameng River in India. Both the SAR and forecast data stemmed from 26 June 2021. Figure 13b shows a similar comparison for the Brahmaputra River in Bangladesh, with SAR data from 13 September 2022 and forecasting information from 12 September 2022. Good correspondence for the SAR-observed and forecasted water extents can be seen, with both data sources indicating similar areas becoming covered by water. Note that the forecast products only captured riverine flooding and did not include the standing water bodies seen in HYDRO30 at locations away from the river.

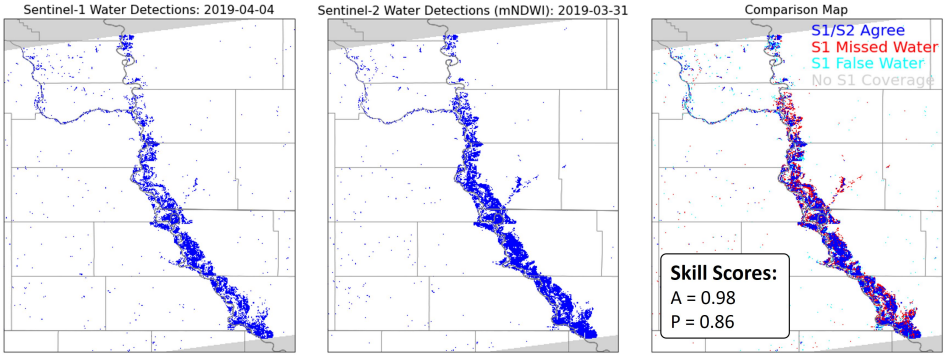

Figure 12. Comparison of HYDRO30 surface water detections of information derived from Sentinel-2 data using the mNDWI. Data acquired over the Missouri River in Nebraska (Sentinel-2 on 4 April 2019; Sentinel-1 on 31 March 2019).

Table 1. Example performance metrics for five pairs of SAR (S1) and optically derived (S2) surface water extent estimates over an area of the Missouri River. SAR water extents were derived using the HyDRO30 algorithm. Optical water detections were extracted using the mNDWI. Acquisition dates are shown for each SAR/optical pair. Data were selected to be within a 5 day window of each other to ensure they measured similar water extents. Accuracy and precision are reported as skill scores. These were calculated by using the optical water detections as a reference.

Skill Score	S1: 04/04 S2: 03/13	S1: 06/27 S2: 06/24	S1: 08/02 S2: 07/19	S1: 08/26 S2: 08/28	S1: 11/13 S2: 11/12
Accuracy	0.98	0.99	0.99	0.99	0.99
Precision	0.79	0.85	0.71	0.64	0.88

These comparisons to multispectral and forecasting data, together with positive feedback from end users in the region, give us confidence in the performance and validity of the HYDRO30 product.

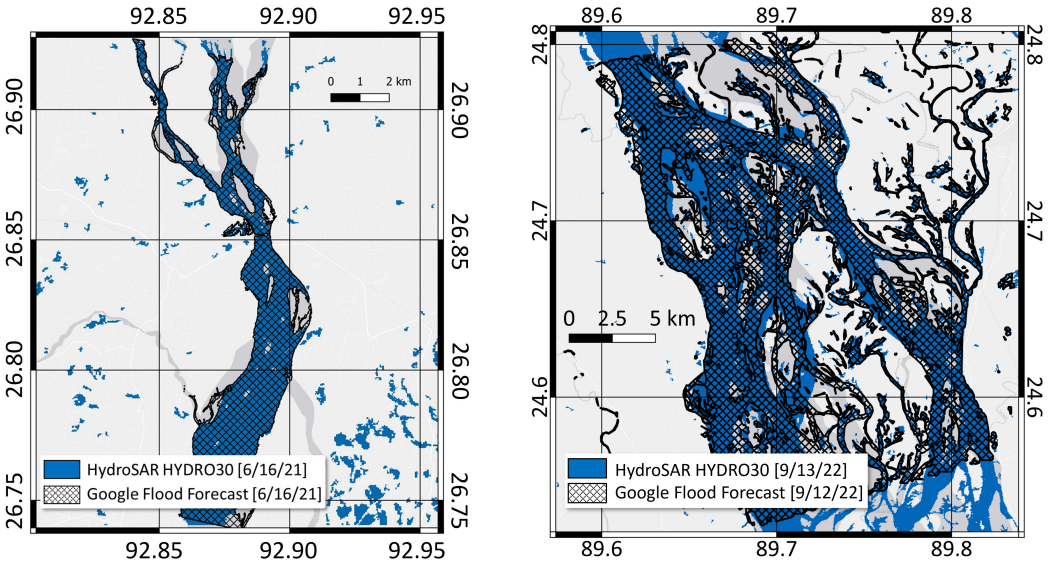

(**a**) (**b**)

Figure 13. Examples of qualitative comparisons of HYDRO30 water extent products (blue) with Google-provided flood forecasts (hash pattern): (**a**) Kameng River in India, with SAR and forecast data from 26 June 2021, and (**b**) Brahmaputra River in Bangladesh, with SAR data from 13 September 2022 and forecast data from 12 September 2022.

7.2. Validating WD30

To evaluate the WD30 products, we used water level data from the Flood Forecasting and Warning Center of the Bangladesh Water Development Board (BWDB) as reference. The BWDB operates 58 gauge stations across Bangladesh and publishes the water levels at these stations through their web interface. We retrieved gauging heights from 11 stations which intersected with our validation area at the confluence of the Padma and Meghna rivers in Bangladesh (Figure 14a). The BWDB's gauging stations use the Public Works Datum (PWD) established in India under British rule. The PWD reference height is roughly 1.5 ft below the mean sea level. We corrected this vertical offset between the BWDB datum and the EGM2008 datum used in the GLO-30 DEM (and therefore the HAND and WD30). Then, the gauge station water heights were compared to the nearest valid WD30 pixel for cross-validation.

Figure 14b shows a comparison of the BWDB gauging heights and WD30 data for our validation site at the confluence of the Padma and Meghna rivers in Bangladesh. Different colored lines correspond to different dates during the 2020 monsoon season for which cross-validation was performed. The R^2 values were close to 0.6 for different dates in 2020. This is because one gauge station, located in an isolated water basin, showed an exceptional range of water levels. If this gauge station were excluded, then an R^2 value near or larger than 0.8 could be observed. Also, a root mean square error (RMSE) of less than 2 m was achieved for each of the analyzed dates. This is in line with the relative vertical accuracy of the Copernicus GLO-30 DEM, which is expected to be better than 2 m in flat terrain (slope $< 20\%$) and better than 4 m in sloping terrain (slope $> 20\%$) [57].

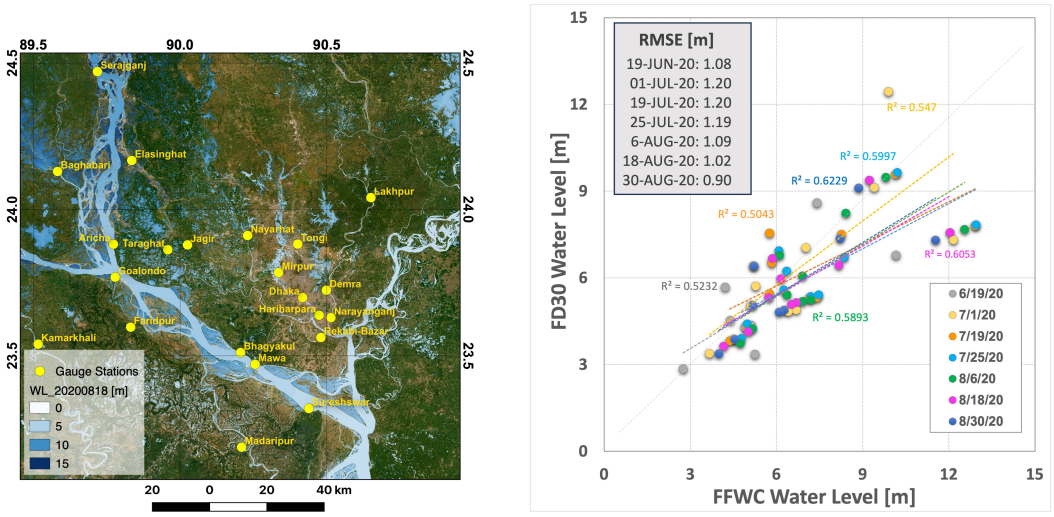

(**a**) (**b**)

Figure 14. WD30 Performance Assessments. (**a**) An example of a SAR-derived water level map and the water level gauge stations in Bangladesh. (**b**) Comparison of WD30 to water level information from the BWDB for the confluence of the Padma and Meghna rivers in Bangladesh. Difference colors correspond to different observation dates.

8. Application Example: 2023 Bangladesh Flooding Season

8.1. Background and Data

Bangladesh is a land of many rivers and, as such, the most flood-susceptible country in the HKH. Sitting at the confluence of three major rivers—the Ganges, Brahmaputra, and Meghnar rivers and their tributaries [58]—Bangladesh faces a number of flood-related risks, such as fluvial flooding due to the accumulation of water from upstream catchments, pluvial flooding due to heavy monsoon rainfalls, and local heavy rainfall enhanced by drainage congestion (Figure 15).

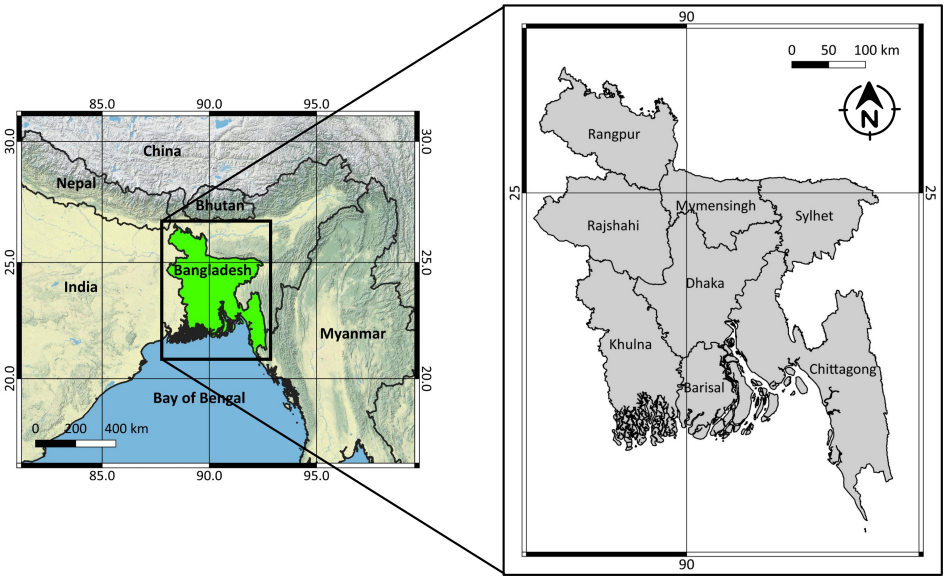

Figure 15. Left: Area of interest (AOI) for countrywide analysis of surface water extent for the flood year 2023. (right) Map of Bangladesh's administrative divisions. These divisions are further analyzed in Section 8.2.

Bangladesh's meteorological year can be divided into three seasons, including the pre-monsoon hot season from March to May, the rainy monsoon season lasting from June to October, and a cool, dry winter season from November to February. The country has an average of 136 wet days per year, and approximately 80% of its yearly rainfall occurs from June to September [4]. Most flooding occurs during the monsoon season, covering up to 31,000 square kilometers or approximately 21% of the country in water. During the most severe flood seasons, up to two-thirds of the country can be covered in water, as was seen during the 1998 monsoon season [59].

Here, we analyze the progression of the 2023 monsoon season for the country of Bangladesh (Figure 15) using operationally generated HydroSAR HYDRO30 data products. The 2023 season was chosen as it was the most recently monitored monsoon season at the time of writing of this article. Furthermore, the 2023 season was impacted by the cyclonic storm Mocha, a powerful and deadly tropical cyclone which made landfall in southern Bangladesh on 14 May 2023. We evaluated the flood extent and flood impacts across the country of Bangladesh as a function of time. All data used in this analysis were retrieved through the ICIMOD's RDS services introduced in Section 5.

A total of 719 Sentinel-1 SAR-derived HYDRO30 products were collected to derive full-coverage surface water extent information in 2 week (14 day) intervals starting on 1 January 2023 and ending on 31 December 2023. A total of 25 14 day flood area maps were compiled from these data. The 14 day integration period was chosen to ensure full wall-to-wall coverage of Bangladesh by Sentinel-1 SAR data. Each 14 day map combined information from an average of 29 individual scenes.

8.2. 2023 Bangladesh Flood Progression

Figure 16 shows the results of a time series analysis of the surface water extent throughout the 2023 Bangladesh flood season, as derived from all available HYDRO30 data. The results show that the surface water extent slowly decreased early in the year as residual water from the previous monsoon season dried up during the dry post-monsoon winter season. A minimum surface water extent of 6549.5 km^2 or 4.42% of the Bangladesh land area was reached on 2 April 2023 near the end of the dry pre-monsoon season. We interpreted this extent as the perennial water extent in Bangladesh.

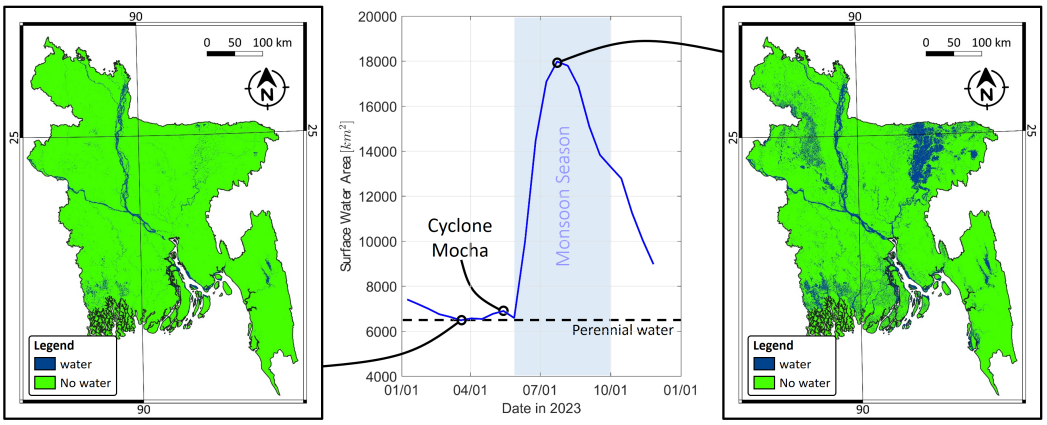

Figure 16. Time series of surface water extent in Bangladesh throughout 2023 as derived from HYDRO30 products. (**left**) Minimum water extent occurring on 2 April 2023. (**middle**) Surface water extent time series. (**right**) Maximum Water extent on 6 August 2023.

A small uptick in water extent can be observed for the time step centered on 14 May 2023. This peak is coincident with the landfall of cyclone Mocha, which caused increased water coverage in Bangladesh's southern divisions of Khulna (southwest) and Chittagong (souteast).

A rapid increase in the water extent commenced around 28 May, marking the onset of the monsoon season. The maximum water extent of 17,138.4 km^2 or 11.6% of the land area was reached near 6 August 2023, marking 2023 as a below-average monsoon season for Bangladesh. After 6 August, the surface water started slowly and progressively receding through the rest of the year.

Bangladesh is divided into eight administrative divisions (Figure 15) that are differently affected by monsoon-related flooding. A division-by-division assessment of the surface water extent (Figure 17) showed that a vast majority of the inundation occurred in the northeastern Sylhet division of Bangladesh. Sylhet is a low-lying area that often acts as a natural "reservoir" for monsoon-related floodwaters. At the peak of the 2023 monsoon season, 31.1% of Sylhet was covered in water. The Chittagong division, located in southeast Bangladesh, showed the lowest surface water area relative to its area (6.7%). This is due to the lack of major rivers draining into this division and due to its higher average topography.

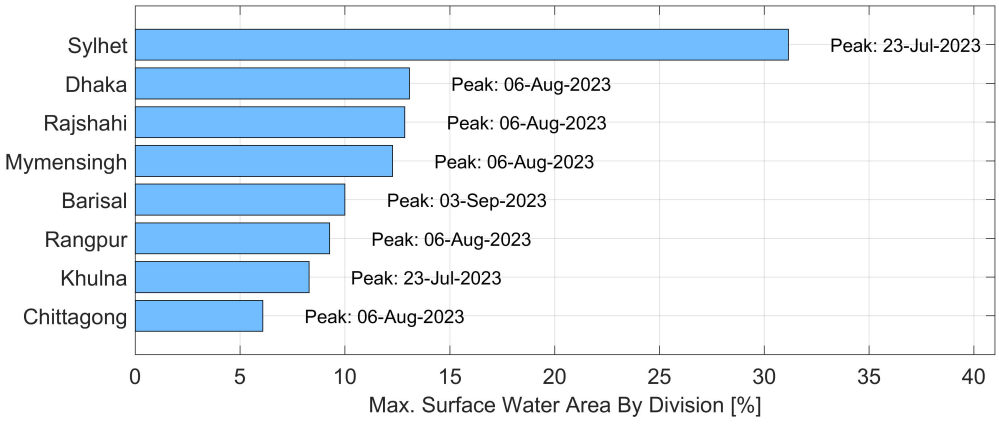

Figure 17. Maximum surface water extent for different divisions of Bangladesh as a percent of the overall division area as calculated from HydroSAR HYDRO30 mosaics.

The available data also allowed determining the timing of the peak water extent for each division (see the text in Figure 17). Our data show that the peak flooding dates were reasonably consistent across Bangladesh, with flood waters peaking near 6 August 2023

in most divisions. The maximum water extent occurred slightly earlier in the Sylhet and Khulna divisions (23 July 2023) and slightly later in Barisal (3 September 2023).

8.3. Total Annual Flood Duration Analysis

How long a particular patch of land was inundated is a relevant metric for assessing the impact of flooding on agricultural crop yields, building integrity, transportation infrastructure, and other landscape functions. Furthermore, it can help in the assessment of the evolution of an inundation event and can be used to support disaster mitigation and prevention by indicating areas most severely affected by floods [15].

We estimated the *total annual flood duration (TAFD)*from our 2023 HydroSAR HYDRO30 data time series by following the approach published in [15]. According to this approach, the TAFD is computed per pixel using all data generated within a calendar year. To provide an accurate count of the inundation days, we allowed for the possibility that a pixel was covered by more than one flood event, accounting for flood-free periods in between. Therefore, similar to [15], we first calculated the duration of each of the n ($n \geq 1$) inundation events separately and then summed all n event durations to arrive at the total flood duration in days:

$$TAFD_i = \sum_{i=1}^{n} D_{d,i} - D_{c,i} \quad (4)$$

where $D_{c,i}$ is the first day and $D_{d,i}$ is the last day inundation was observed for an event i.

Figure 18a shows the results of this analysis for the 2023 flood season. For ease of visualization, the TAFD results were divided into four categories: white pixels were never inundated; green areas were inundated for less than 30 days; red areas were inundated for $\geq$30 and $<$100 days; and blue pixels were water-covered for $>$100 and $<$200 davs.

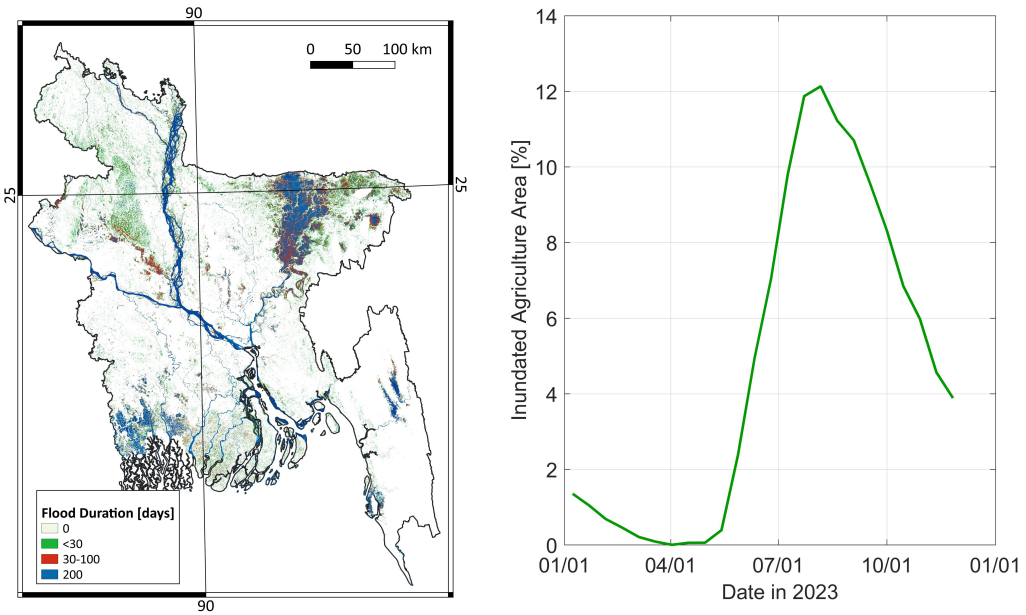

(**a**) (**b**)

Figure 18. Total annual flood duration and flood−impacted agriculture areas. (**a**) Total annual flood duration (TAFD) per pixel, as calculated from HYDRO30 time series. Data were categorized into four classes as shown in the legend. (**b**) Extent of flood−impacted agriculture areas as a function of time, calculated by intersecting HYDRO30 information with agriculture extent information extracted from the Copernicus Global Land Monitoring Service.

It can be seen that large areas of the low-lying Sylhet division in northeastern Bangladesh were water-covered for more than 100 days. Long-lasting inundation can also be observed

for some areas of the southwestern Khulna division. Note that permanent water was included in this category.

Areas affected by short-duration (less than 30 days) flooding can be found throughout the country but occur most prominently in the Rajshahi and Rangpur divisions, as well as in the Mymensingh, Barisal, and Sylhet divisions.

8.4. Affected Agriculture Areas

As HydroSAR's AG30 agriculture extent product is not yet fully operational and implemented, we used Dynamic Land Cover Product version 3, distributed by the Copernicus Global Land Monitoring Service [36], to assess the impact of the 2023 flood season on Bangladesh's agriculture regions. This 100 m resolution product offers annual global land cover information derived from observations of the PROBA-V satellite [60]. The latest version of this product was assessed to achieve a classification accuracy of 80% on each continent [36]. We extracted the agriculture extent information from this product and resampled the extracted layer to match the posting of the HYDRO30 products for further joint analysis.

We first derived the time series of agriculture inundation by intersecting the agriculture extent layer with the bi-weekly HYDRO30 surface water extent information. The results of this analysis are shown in Figure 18b. Similar to the water extent time series in Figure 16, we observed the minimum inundated agriculture in early April. Agriculture inundation started to increase with the onset of the monsoon and reached a maximum on 6 August 2023, where 13.5% of all agriculture lands were identified as water-covered. Inundation dropped rapidly after this date as monsoon waters began to recede.

In flood situations, the extent of crop damage and therefore the impact on crop yield often depends on the duration of flooding. To study how long Bangladesh's flood-affected agriculture lands were inundated, we could intersect the Copernicus agriculture extent information with the TAFD layer, as shown in Figure 18a. Note that this analysis would reveal how long a certain agriculture patch was inundated but did not allow assessing when this inundation occurred.

Figure 19 shows that 11.2% of Bangladesh's agriculture areas were inundated for 30 days or less, where 5.3% of the crop lands were inundated for between 30 and 100 days and 4.6% of Bangladesh's agriculture areas were inundated for more than 100 days. Combined with information about crop types, these data could help in the evaluation of flood impacts on food production.

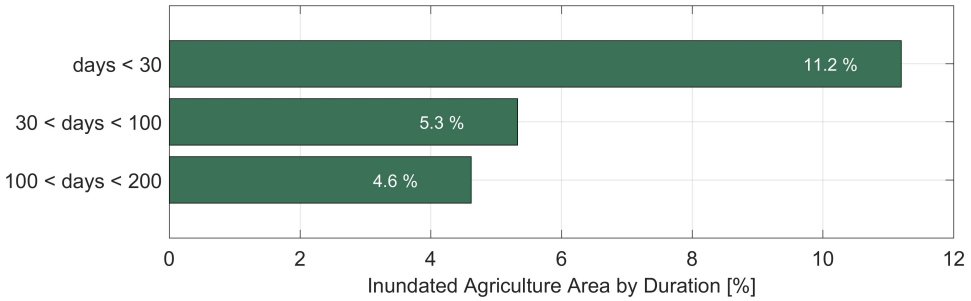

Figure 19. Agriculture areas covered in water as a function of flooding duration, calculated by intersecting AG with TAFD.

The examples shown in Section 8 provide some indication of the value of the HydroSAR service for flood analysis in the region. Beyond the retrospective studies shown here, HydroSAR data can be used a range of other applications, such as the analysis of individual flooding events or the statistical analysis of multiple years of data in support of flood mitigation.

9. Summary and Conclusions

We collaborated closely with partners in the HKH to develop HydroSAR, an SAR data processing and analysis service focused on the automatic, year-round, and near real-time generation of flood information products for this region. To meet end user needs, HydroSAR was designed with a broad product suite in mind, which enables the simultaneous assessment of several flood-related parameters as events unfold and progress. The service uses Sentinel-1 SAR data as its input and is fully cloud-based to enable rapid product generation at scale. A tight integration with ASF's cloud-based Sentinel-1 SAR archives ensures that data do not have to be migrated out of the cloud, maximizing the throughput and minimizing processing costs.

The service was successfully transitioned to ICIMOD, a regional organization in the HKH who continue to operate HydroSAR and provide its data to end users through a dedicated web portal. An application of HydroSAR to analyze the 2023 southeast Asia monsoon season showcased one of many potential use cases of HydroSAR and demonstrated the amount of information which can be extracted from the available data.

The HydroSAR team has been monitoring the performance of its service since operational data production started in 2022. These analyses have revealed a number of strengths and limitations of the service. The service has demonstrated rapid and fully automatic data production capabilities, resulting in the consistent, weather-independent, and continuous delivery of low-latency flood hazard information to the region. Regular spot checks of the data quality and positive feedback from end users indicated improved capabilities in monitoring monsoon-related flood hazards, especially for the regions of Bangladesh, northern India, southern Nepal, and southern Bhutan. The temporal sampling provided by the service was found to be sufficient to monitor the emergence and recession of monsoon-related waters on a regional scale.

Some limitations of the service were found to be related to the side-looking geometry of SAR, which has resulted in limited visibility for some of the narrower mountain valleys of Nepal. The 30 m resolution of HydroSAR data products has also resulted in occasional missed detections in areas where rivers are narrower than the 30 m pixel size. Finally, while the temporal sampling of our Sentinel-1-backed service has been sufficient for monitoring slowly evolving monsoon floods, it has not been a reliable resource for the assessment of flash flooding events in the region. These rapidly unfolding events are a growing risk in the HKH [61] but often evade detection from spaceborne sensors.

The team continues to work with its partners to address these identified challenges and improve the service. We are currently evaluating the benefits of moving to a 20 m product for areas in Nepal where 30 m data revealed challenges with monitoring narrow rivers. We are also preparing for the integration of data from the highly anticipated NASA-ISRO SAR (NISAR) mission, which is currently scheduled for launch in early 2025. Finally, we are investigating machine learning algorithms, which would combine SAR data with river discharge forecasts to enable daily flood water extent forecasting.

Author Contributions: Conceptualization, F.J.M. and R.B.T.; methodology, F.J.M., B.O., M.J., J.H.K., J.R.B., B.K. and L.A.S.; software, F.J.M., B.O., M.J., J.H.K., J.R.B., T.J.M. and J.S.; validation, F.J.M., M.J., M.S., T.J.M. and L.A.S.; formal analysis, F.J.M. and B.O.; investigation, F.J.M.; resources, F.J.M.; data curation, J.H.K., H.K. and S.P.; writing—original draft preparation, F.J.M.; writing—review and editing, B.O., M.J., R.B.T., J.H.K. and L.A.S.; visualization, F.J.M., M.J., H.K., M.S. and R.B.T.; supervision, F.J.M., B.O. and L.A.S.; project administration, F.J.M.; funding acquisition, F.J.M. All authors have read and agreed to the published version of the manuscript.

Funding: This research was funded by the NASA Science Mission Directorate under grant numbers 80NSSC20K0164 and 80NSSC19K1109.

Data Availability Statement: All data presented in this report are openly accessible through the ICIMOD Flood Inundation portal at https://geoapps.icimod.org/Floodinundation/ (accessed on 26 August 2024) and can be downloaded through the ICIMOD Regional Database System (RDS) (https://rds.icimod.org/Home/DataDetail?metadataId=1973127) (accessed on 26 August 2024). The

software implementations of all HydroSAR algorithms are available from an open GitHub repository at https://github.com/HydroSAR/HydroSAR (accessed on 12 August 2024).

Acknowledgments: Products provided by the HydroSAR service are derived from Copernicus Sentinel data processed by the ESA. Sentinel-1 data were accessed through the services of the Distributed Active Archive Center (DAAC) of NASA's Alaska Satellite Facility (ASF). We thank the ASF HyP3 (https://hyp3-docs.asf.alaska.edu/, accessed on 12 August 2024) team for their support with the cloud implementation of our workflows. We owe gratitude to the team at the NASA SERVIR Science Coordination Office for their support and guidance. We thank our partners at the ICIMOD and their connected end users for their input and collaboration.

Conflicts of Interest: The authors declare no conflicts of interest.

References

1. Vaidya, R.A.; Shrestha, M.S.; Nasab, N.; Gurung, D.R.; Kozo, N.; Pradhan, N.S.; Wasson, R.J. Disaster risk reduction and building resilience in the Hindu Kush Himalaya. In *The Hindu Kush Himalaya Assessment: Mountains, Climate Change, Sustainability and People*; Springer: Cham, Switzerland, 2019; pp. 389–419.
2. Bajracharya, B.; Thapa, R.B.; Matin, M.A. *Earth Observation Science and Applications for Risk Reduction and Enhanced Resilience in Hindu Kush Himalaya Region: A Decade of Experience from SERVIR*; Springer Nature: Cham, Switzerland, 2021.
3. Shrestha, M.S.; Grabs, W.E.; Khadgi, V.R. Establishment of a regional flood information system in the Hindu Kush Himalayas: Challenges and opportunities. *Int. J. Water Resour. Dev.* **2015**, *31*, 238–252. [CrossRef]
4. Uddin, K.; Matin, M.A.; Meyer, F.J. Operational flood mapping using multi-temporal Sentinel-1 SAR images: A case study from Bangladesh. *Remote Sens.* **2019**, *11*, 1581. [CrossRef]
5. Potin, P.; Bargellini, P.; Laur, H.; Rosich, B.; Schmuck, S. Sentinel-1 mission operations concept. In Proceedings of the 2012 IEEE International Geoscience and Remote Sensing Symposium, Munich, Germany, 22–27 July 2012; pp. 1745–1748.
6. Kellogg, K.; Hoffman, P.; Standley, S.; Shaffer, S.; Rosen, P.; Edelstein, W.; Dunn, C.; Baker, C.; Barela, P.; Shen, Y.; et al. NASA-ISRO synthetic aperture radar (NISAR) mission. In Proceedings of the 2020 IEEE Aerospace Conference, Big Sky, MT, USA, 7–14 March 2020; pp. 1–21.
7. Martinis, S.; Twele, A.; Voigt, S. Towards operational near real-time flood detection using a split-based automatic thresholding procedure on high resolution TerraSAR-X data. *Nat. Hazards Earth Syst. Sci.* **2009**, *9*, 303–314. [CrossRef]
8. Long, S.; Fatoyinbo, T.E.; Policelli, F. Flood extent mapping for Namibia using change detection and thresholding with SAR. *Environ. Res. Lett.* **2014**, *9*, 035002. [CrossRef]
9. Seitz, F.; Hedman, K.; Meyer, F.J.; Lee, H. Multi-sensor space observation of heavy flood and drought conditions in the Amazon region. In *Earth on the Edge: Science for a Sustainable Planet: Proceedings of the IAG General Assembly, Melbourne, Australia, 28 June–2 July 2011*; Springer: Berlin/Heidelberg, Germany, 2014; pp. 311–317.
10. Meyer, F.; McAlpin, D.; Gong, W.; Ajadi, O.; Arko, S.; Webley, P.; Dehn, J. Integrating SAR and derived products into operational volcano monitoring and decision support systems. *ISPRS J. Photogramm. Remote Sens.* **2015**, *100*, 106–117. [CrossRef]
11. Ajadi, O.A.; Meyer, F.J.; Webley, P.W. Change detection in synthetic aperture radar images using a multiscale-driven approach. *Remote Sens.* **2016**, *8*, 482. [CrossRef]
12. Twele, A.; Cao, W.; Plank, S.; Martinis, S. Sentinel-1-based flood mapping: A fully automated processing chain. *Int. J. Remote Sens.* **2016**, *37*, 2990–3004. [CrossRef]
13. Tran, K.H.; Menenti, M.; Jia, L. Surface water mapping and flood monitoring in the Mekong Delta using sentinel-1 SAR time series and Otsu threshold. *Remote Sens.* **2022**, *14*, 5721. [CrossRef]
14. Qiu, J.; Cao, B.; Park, E.; Yang, X.; Zhang, W.; Tarolli, P. Flood monitoring in rural areas of the Pearl River Basin (China) using Sentinel-1 SAR. *Remote Sens.* **2021**, *13*, 1384. [CrossRef]
15. Martinis, S.; Wieland, M.; Rättich, M. An Automatic System for Near-Real Time Flood Extent and Duration Mapping Based on Multi-Sensor Satellite Data. In *Earth Observation for Flood Applications*; Elsevier: Amsterdam, The Netherlands, 2021; pp. 7–37.
16. Otsu, N. A threshold selection method from gray-level histograms. *Automatica* **1975**, *11*, 23–27. [CrossRef]
17. Uddin, K.; Matin, M.A.; Thapa, R.B. Rapid flood mapping using multi-temporal sar images: An example from Bangladesh. In *A Decade of Experience from SERVIR*; Springer: Cham, Switzerland, 2021; p. 201.
18. Aziz, M.A.; Moniruzzaman, M.; Tripathi, A.; Hossain, M.I.; Ahmed, S.; Rahaman, K.R.; Rahman, F.; Ahmed, R. Delineating flood zones upon employing synthetic aperture data for the 2020 flood in Bangladesh. *Earth Syst. Environ.* **2022**, *6*, 733–743. [CrossRef]
19. Singha, M.; Dong, J.; Sarmah, S.; You, N.; Zhou, Y.; Zhang, G.; Doughty, R.; Xiao, X. Identifying floods and flood-affected paddy rice fields in Bangladesh based on Sentinel-1 imagery and Google Earth Engine. *ISPRS J. Photogramm. Remote Sens.* **2020**, *166*, 278–293. [CrossRef]
20. Pandey, A.C.; Kaushik, K.; Parida, B.R. Google Earth Engine for large-scale flood mapping using SAR data and impact assessment on agriculture and population of Ganga-Brahmaputra basin. *Sustainability* **2022**, *14*, 4210. [CrossRef]
21. Soria-Ruiz, J.; Fernandez-Ordoñez, Y.M.; Ambrosio-Ambrosio, J.P.; Escalona-Maurice, M.J.; Medina-García, G.; Sotelo-Ruiz, E.D.; Ramirez-Guzman, M.E. Flooded extent and depth analysis using optical and SAR remote sensing with machine learning algorithms. *Atmosphere* **2022**, *13*, 1852. [CrossRef]

22. Hao, C.; Yunus, A.P.; Subramanian, S.S.; Avtar, R. Basin-wide flood depth and exposure mapping from SAR images and machine learning models. *J. Environ. Manag.* **2021**, *297*, 113367. [CrossRef]
23. Delaney, K.B.; Evans, S.G. The evolution (2010–2015) and engineering mitigation of a rockslide-dammed lake (Hunza River, Pakistan); characterisation by analytical remote sensing. *Eng. Geol.* **2017**, *220*, 65–75. [CrossRef]
24. Surampudi, S.; Kumar, V. Flood depth estimation in agricultural lands from L and C-band synthetic aperture radar images and digital elevation model. *IEEE Access* **2023**, *11*, 3241–3256. [CrossRef]
25. Ozaki, M. *Disaster Risk Financing in Bangladesh*; Working Paper Series; Asian Development Bank: Metro Manila, Philippines, 2016.
26. Hussain, A.; Rasul, G.; Mahapatra, B.; Tuladhar, S. Household food security in the face of climate change in the Hindu-Kush Himalayan region. *Food Secur.* **2016**, *8*, 921–937. [CrossRef]
27. Manjusree, P.; Prasanna Kumar, L.; Bhatt, C.M.; Rao, G.S.; Bhanumurthy, V. Optimization of threshold ranges for rapid flood inundation mapping by evaluating backscatter profiles of high incidence angle SAR images. *Int. J. Disaster Risk Sci.* **2012**, *3*, 113–122. [CrossRef]
28. Thapa, R.B.; Bajracharya, B.; Matin, M.A.; Anderson, E.; Epanchin, P. Service planning approach and its application. In *A Decade of Experience from SERVIR*; Springer: Cham, Switzerland, 2021, p. 23.
29. Molden, D.; Sharma, E. ICIMOD's strategy for delivering high-quality research and achieving impact for sustainable mountain development. *Mt. Res. Dev.* **2013**, *33*, 179–183. [CrossRef]
30. Cigna, F.; Xie, H. Imaging floods and glacier geohazards with remote sensing. *Remote Sens.* **2020**, *12*, 3874. [CrossRef]
31. Bell, J.; Kubby, B.; Meyer, F.; Yadav, S. Identifying and Mapping Agricultural Areas Using Synthetic Aperture Radar Time Series. In Proceedings of the AGU Fall Meeting, New Orleans, LA, USA, 13–17 December 2021; Volume 2021, p. GC45I-0925.
32. Copernicus DEM. 2022. Available online: https://dataspace.copernicus.eu/explore-data/data-collections/copernicus-contributing-missions/collections-description/COP-DEM (accessed on 3 March 2024).
33. Zink, M.; Moreira, A.; Hajnsek, I.; Rizzoli, P.; Bachmann, M.; Kahle, R.; Fritz, T.; Huber, M.; Krieger, G.; Lachaise, M.; et al. TanDEM-X: 10 years of formation flying bistatic SAR interferometry. *IEEE J. Sel. Top. Appl. Earth Obs. Remote Sens.* **2021**, *14*, 3546–3565. [CrossRef]
34. Wessel, B.; Huber, M.; Wohlfart, C.; Marschalk, U.; Kosmann, D.; Roth, A. Accuracy assessment of the global TanDEM-X Digital Elevation Model with GPS data. *ISPRS J. Photogramm. Remote Sens.* **2018**, *139*, 171–182. [CrossRef]
35. Lehner, B.; Verdin, K.; Jarvis, A. New global hydrography derived from spaceborne elevation data. *Eos Trans. Am. Geophys. Union* **2008**, *89*, 93–94. [CrossRef]
36. Buchhorn, M.; Lesiv, M.; Tsendbazar, N.E.; Herold, M.; Bertels, L.; Smets, B. Copernicus global land cover layers—Collection 2. *Remote Sens.* **2020**, *12*, 1044. [CrossRef]
37. Nobre, A.D.; Cuartas, L.A.; Hodnett, M.; Rennó, C.D.; Rodrigues, G.; Silveira, A.; Saleska, S. Height Above the Nearest Drainage—A hydrologically relevant new terrain model. *J. Hydrol.* **2011**, *404*, 13–29. [CrossRef]
38. Gharari, S.; Hrachowitz, M.; Fenicia, F.; Savenije, H.H.G. Hydrological landscape classification: Investigating the performance of HAND based landscape classifications in a central European meso-scale catchment. *Hydrol. Earth Syst. Sci.* **2011**, *15*, 3275–3291. [CrossRef]
39. Hogenson, K.; Kristenson, H.; Kennedy, J.; Johnston, A.; Rine, J.; Logan, T.; Zhu, J.; Williams, F.; Herrmann, J.; Smale, J.; et al. *Hybrid Pluggable Processing Pipeline (HyP3): A Cloud-Native Infrastructure for Generic Processing of SAR Data*; Zenodo: Geneva, Switzerland, 2024. [CrossRef]
40. Small, D.; Zuberbühler, L.; Schubert, A.; Meier, E. Terrain-flattened gamma nought Radarsat-2 backscatter. *Can. J. Remote Sens.* **2011**, *37*, 493–499. [CrossRef]
41. Shiroma, G.H.; Lavalle, M.; Buckley, S.M. An area-based projection algorithm for SAR radiometric terrain correction and geocoding. *IEEE Trans. Geosci. Remote Sens.* **2022**, *60*, 1–23. [CrossRef]
42. Small, D. Flattening gamma: Radiometric terrain correction for SAR imagery. *IEEE Trans. Geosci. Remote Sens.* **2011**, *49*, 3081–3093. [CrossRef]
43. Flores-Anderson, A.I.; Parache, H.B.; Martin-Arias, V.; Jiménez, S.A.; Herndon, K.; Mehlich, S.; Meyer, F.J.; Agarwal, S.; Ilyushchenko, S.; Agarwal, M.; et al. Evaluating SAR Radiometric Terrain Correction Products: Analysis-Ready Data for Users. *Remote Sens.* **2023**, *15*, 5110. [CrossRef]
44. Truckenbrodt, J.; Freemantle, T.; Williams, C.; Jones, T.; Small, D.; Dubois, C.; Thiel, C.; Rossi, C.; Syriou, A.; Giuliani, G. Towards Sentinel-1 SAR analysis-ready data: A best practices assessment on preparing backscatter data for the cube. *Data* **2019**, *4*, 93. [CrossRef]
45. Nicolau, A.P.; Flores-Anderson, A.; Griffin, R.; Herndon, K.; Meyer, F.J. Assessing SAR C-band data to effectively distinguish modified land uses in a heavily disturbed Amazon forest. *Int. J. Appl. Earth Obs. Geoinf.* **2021**, *94*, 102214. [CrossRef]
46. Frey, O.; Santoro, M.; Werner, C.L.; Wegmuller, U. DEM-based SAR pixel-area estimation for enhanced geocoding refinement and radiometric normalization. *IEEE Geosci. Remote Sens. Lett.* **2012**, *10*, 48–52. [CrossRef]
47. Martinis, S.; Kersten, J.; Twele, A. A fully automated TerraSAR-X based flood service. *ISPRS J. Photogramm. Remote Sens.* **2015**, *104*, 203–212. [CrossRef]
48. Sciance, M.B.; Nooner, S.L. Decadal flood trends in Bangladesh from extensive hydrographic data. *Nat. Hazards* **2018**, *90*, 115–135. [CrossRef]

49. Meyer, F.J.; Schultz, L.; Bell, J.; Molthan, A.L.; Osmanoglu, B.; Jo, M.; Lundell, E.; Chapman, B.D.; Kubby, B.; Meyer, T.; et al. Monitoring Weather-Related Hazards Using the HydroSAR Service: Application to the 2020 South Asia Monsoon Season. In Proceedings of the 2021 IEEE International Geoscience and Remote Sensing Symposium IGARSS, Brussels, Belgium, 11–16 July 2021; pp. 893–896.
50. Pekel, J.F.; Cottam, A.; Gorelick, N.; Belward, A.S. High-resolution mapping of global surface water and its long-term changes. *Nature* **2016**, *540*, 418–422. [CrossRef]
51. Olson, B.; Shehu, A. Efficient basin hopping in the protein energy surface. In Proceedings of the 2012 IEEE International Conference on Bioinformatics and Biomedicine, Philadelphia, PA, USA, 4–7 October 2012; pp. 1–6.
52. Hogenson, K.; Arko, S.A.; Buechler, B.; Hogenson, R.; Herrmann, J.; Geiger, A. Hybrid Pluggable Processing Pipeline (HyP3): A cloud-based infrastructure for generic processing of SAR data. In Proceedings of the AGU Fall Meeting, San Francisco, CA, USA, 12–16 December 2016; Volume 2016, p. IN21B-1740.
53. Rad, B.B.; Bhatti, H.J.; Ahmadi, M. An introduction to docker and analysis of its performance. *Int. J. Comput. Sci. Netw. Secur. (IJCSNS)* **2017**, *17*, 228.
54. Nevo, S.; Morin, E.; Gerzi Rosenthal, A.; Metzger, A.; Barshai, C.; Weitzner, D.; Voloshin, D.; Kratzert, F.; Elidan, G.; Dror, G.; et al. Flood forecasting with machine learning models in an operational framework. *Hydrol. Earth Syst. Sci.* **2022**, *26*, 4013–4032. [CrossRef]
55. Pal, S.; Lee, T.R.; Clark, N.E. The 2019 Mississippi and Missouri River flooding and its impact on atmospheric boundary layer dynamics. *Geophys. Res. Lett.* **2020**, *47*, e2019GL086933. [CrossRef]
56. Xu, H. Modification of normalised difference water index (NDWI) to enhance open water features in remotely sensed imagery. *Int. J. Remote Sens.* **2006**, *27*, 3025–3033. [CrossRef]
57. Fahrland, E.; Jacob, P.; Schrader, H.; Kahabka, H. *Copernicus Digital Elevation Model—Product Handbook*; Airbus Defence and Space—Intelligence: Potsdam, Germany, 2020.
58. Haque, M.N.; Siddika, S.; Sresto, M.A.; Saroar, M.M.; Shabab, K.R. Geo-spatial analysis for flash flood susceptibility mapping in the North-East Haor (Wetland) Region in Bangladesh. *Earth Syst. Environ.* **2021**, *5*, 365–384. [CrossRef]
59. AM, D.; Nishigaki, M.; Komatsu, M. Floods in Bangladesh: A comparative hydrological investigation on two catastrophic events. *J. Fac. Environ. Sci. Technol.* **2003**, *8*, 53–62.
60. Francois, M.; Santandrea, S.; Mellab, K.; Vrancken, D.; Versluys, J. The PROBA-V mission: The space segment. *Int. J. Remote Sens.* **2014**, *35*, 2548–2564. [CrossRef]
61. Poudel, K.R.; Hamal, R. Assessment of Natural Hazard in the Himalayas: A Case Study of the Seti River Flash Flood 2012. *Prithvi J. Res. Innov.* **2021**, *3*, 12–25. [CrossRef]